

# U–Pb SHRIMP zircon geochronology and $T-t-d$ history of the Kampa Dome, southern Tibet

M.C. Quigley<sup>a,\*</sup>, Y. Liangjun<sup>b</sup>, C. Gregory<sup>c</sup>, A. Corvino<sup>a</sup>, M. Sandiford<sup>a</sup>,  
C.J.L. Wilson<sup>a</sup>, L. Xiaohan<sup>b</sup>

<sup>a</sup> School of Earth Sciences, The University of Melbourne, Australia 3010

<sup>b</sup> Institute of Geology and Geophysics, Chinese Academy of Sciences, Beijing, China 100029

<sup>c</sup> Research School of Earth Sciences, The Australia National University, Canberra, Australia 0200

Received 5 September 2007; received in revised form 25 October 2007; accepted 3 November 2007

Available online 17 November 2007

## Abstract

Structural, petrographic and geochronologic studies of the Kampa Dome provide insights into the tectonothermal evolution of orogenic crust exposed in the North Himalayan gneiss domes of southern Tibet. U–Pb ion microprobe dating of zircons from granite gneiss exposed at the deepest levels within the dome yields concordia  $^{206}\text{Pb}/^{238}\text{U}$  age populations of  $506 \pm 3$  Ma and  $527 \pm 6$  Ma, with no evidence of new zircon growth during Himalayan orogenesis. However, the granite contains penetrative deformation fabrics that are also preserved in the overlying Paleozoic strata, implying that the Kampa granite is a Cambrian pluton that was strongly deformed and metamorphosed during Himalayan orogenesis. Zircons from deformed leucogranite sills that cross-cut Paleozoic metasedimentary rocks yield discordant Cambrian ages from oscillatory zoned cores and discordant ages ranging from ca. 491–32 Ma in metamict grains. Since these leucogranites clearly post-date the metasedimentary rocks they intrude, the zircons are interpreted as xenocrysts that are probably derived from the Kampa granite. The Kampa Dome formed via a series of progressive orogenic events including regional ~N–S contraction and related crustal thickening ( $D_1$ ), predominately top-to-N ductile shearing and crustal extension ( $D_2$ ), top-to-N brittle–ductile faulting and related folding on the north limb of the dome, localized top-to-S faulting on the southern limb of the dome, and crustal doming ( $D_3$ ), and continued N–S contraction, E–W extension and doming ( $D_4$ ). Structural and geochronologic variability amongst adjacent North Himalayan gneiss domes may reflect changes in the magnitude of crustal exhumation along the North Himalayan antiform, possibly relating to differences in the mid-crustal geometry of the exhuming fault systems.

© 2007 Elsevier B.V. All rights reserved.

**Keywords:** Gneiss domes; Channel flow; Structural geology; U–Pb SHRIMP geochronology; Himalaya; Tibet

## 1. Introduction

The North Himalayan gneiss domes (NHGD) in southern Tibet (Fig. 1) contain high-grade metamorphic and intrusive rocks that provide a record of Himalayan–Tibetan orogenesis (e.g., Burg et al., 1984; Debon et al., 1986; Chen et al., 1990; Lee et al., 2000, 2004; Zhang et al., 2004; Aoya et al., 2005, 2006; Quigley et al., 2006; Lee et al., 2006). Several workers have proposed that rocks presently exposed in the cores of the NHGD formed part of a mid-crustal channel that was laterally

continuous with the Greater Himalayan Sequence during the Oligo-Miocene (Hauck et al., 1998; Beaumont et al., 2001, 2004; Lee et al., 2006; Lee and Whitehouse, 2007). The NHGD therefore provide an opportunity to investigate the mid-crustal processes involved in continental orogenesis and to evaluate the hypothesis that weak mid-crustal layers in orogenic belts may flow laterally and be linked to surface denudation (i.e. ‘Channel flow’; Beaumont et al., 2001).

Recent studies have highlighted both the similarities and differences amongst the NHGD exposed along the North Himalayan antiform (Fig. 1) (e.g., Lee et al., 2006; Kawakami et al., 2007). One important difference among the NHGD concerns the age and origin of granitic rocks exposed in the domal

\* Corresponding author. Tel.: +61 3 8344 7542; fax: +61 3 8344 7761.

E-mail address: [mquigley@unimelb.edu.au](mailto:mquigley@unimelb.edu.au) (M.C. Quigley).

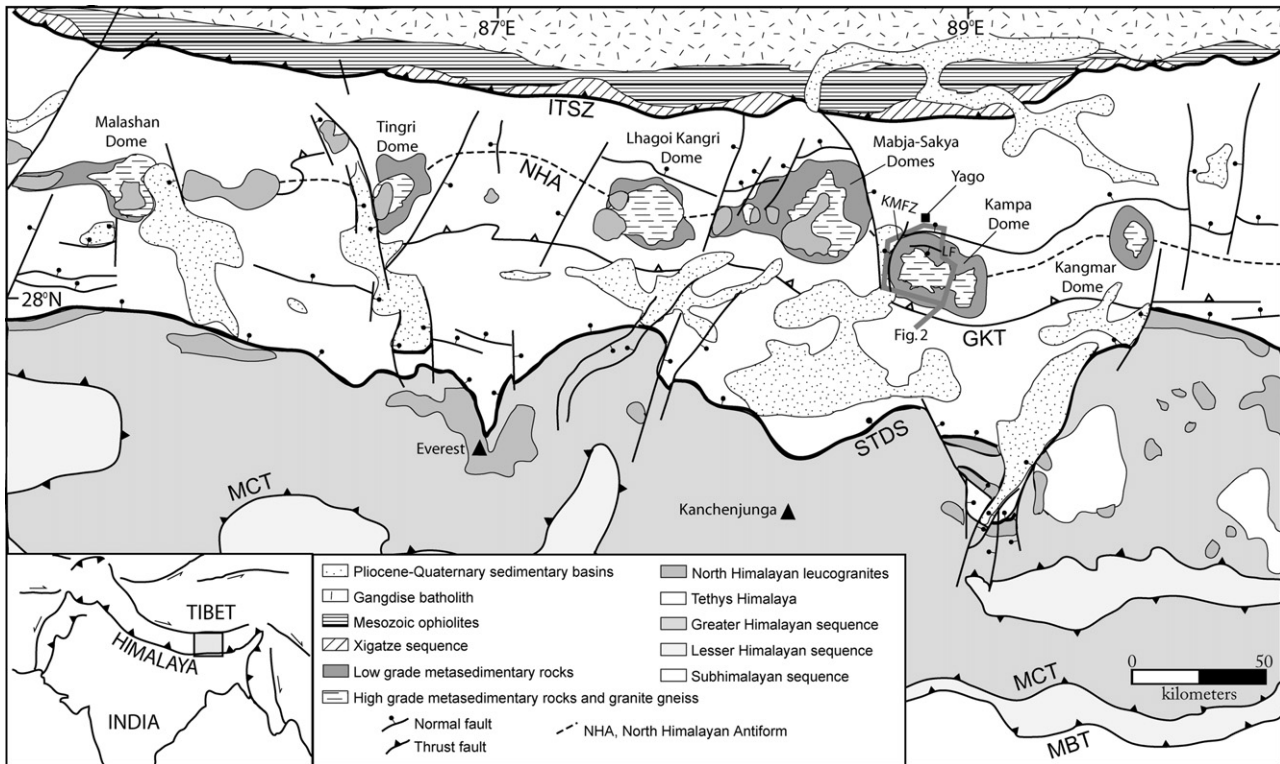


Fig. 1. Regional tectonic map of the central Himalayan orogen including the North Himalayan gneiss domes, modified from Burchfiel et al. (1992), Burg (1983), Watts et al. (2005), and Zengquian et al. (1986). MBT, Main Boundary Thrust; MCT, Main Central Thrust; STDs, South Tibetan Detachment System; GKT, Gyirom–Kangmar Thrust; NHA, North Himalayan antiform; ITSZ, Indus–Tsangpo Suture Zone. Location of Fig. 2 map shown by grey outline in the western Kampa Dome. Inset map shows location of regional map, modified from Burchfiel et al. (1992).

cores. Granitic gneiss exposed in the core of the Kangmar Dome yields Cambrian U–Pb zircon ages (Table 1) (Schärer et al., 1986; Lee et al., 2000), implying that the rocks coring this dome were metamorphosed and deformed during Himalayan orogenesis without additional zircon growth. Migmatites, pegmatites, and undeformed granites in the Mabja Dome contain zircons with Cambrian cores, but Tertiary rims (Lee and Whitehouse, 2007). These authors attributed rim growth in the migmatites to metamorphism and rim growth in the pegmatites and undeformed granites to new igneous growth. The granite gneiss exposed in the core of Malashan Dome (Fig. 1) yields U–Pb zircon core ages of 908 Ma to 250 Ma with predominantly Miocene rim ages (Table 1) (Aoya et al., 2006; Kawakami et al., 2007). The Miocene rim ages were interpreted to indicate the timing of granite emplacement (Aoya et al., 2006). Because the Kangmar and Malashan granites have very similar geologic, textural and bulk chemical characteristics, Aoya et al. (2006) hypothesized that deformed granites within the NHGD, including the Kangmar granite, are Himalayan intrusions (i.e. magma bodies that were emplaced into the Tethyan sequence following initial India–Asia collision at ~55–34 Ma; Klootwijk et al., 1992; Aitchison et al., 2007). Resolving this controversy is critical because interpretation of many of the primary features of the domes, including the spatial and temporal patterns of metamorphism and deformation in the metasedimentary sequence, relies heavily on interpretations of the age and origin of the underlying orthogneiss. For instance, Aoya et al. (2005, 2006) attributed the formation of a metamorphic aureole in the Malashan Dome to contact metamorphism

associated with the emplacement of the Malashan granite, and suggested that granite emplacement triggered the onset of extensional tectonics in southern Tibet (e.g., Lee et al., 2004). A contact metamorphic aureole is also well-preserved in Mabja and its age is similar to that documented in Malashan (Lee et al., 2004). Conversely, Lee et al. (2000) attributed peak metamorphism of the metasedimentary sequence in Kangmar to thermal re-equilibration following a period of crustal thickening, and emphasized that the Kangmar granite was not the heat source for the metamorphism.

The second difference between the domes concerns the nature of the contact between the orthogneiss core of the gneiss domes and the overlying metasedimentary mantle. In the Kangmar Dome, this contact has been variably interpreted as an unconformity (Burg et al., 1984; Zhang et al., 1986), an intrusive contact (Zhou et al., 1981), a metamorphic core complex-type detachment fault (Chen et al., 1990), and a nonconformity across which there has been minimal brittle displacement (Lee et al., 2000). In the Malashan Dome, this contact is interpreted as an intrusive contact that was modified by subsequent deformation (Wallis et al., 2004; Aoya et al., 2006; Kawakami et al., 2007). Resolving the nature of this contact, as well as the deformational kinematics preserved in overlying and underlying rocks is of fundamental importance to distinguishing between proposed dome-forming mechanisms, including contraction and thrust duplexing (Burg et al., 1984), extension (Chen et al., 1990), diapirism (Le Fort, 1986; Le Fort et al., 1987), coeval upper crustal thinning and emergence of a southward flowing mid-

Table 1  
Compiled U-Pb geochronology from NHGD

Dome	Lithology	Age (Ma)	Technique	Reference
Kangmar	Deformed granite orthogneiss	562±4	U-Pb-zircon	Schärer et al. (1986)
	Deformed granite orthogneiss	508±1	U-Pb-zircon	Lee et al. (2000)
Kampa	Deformed granite orthogneiss	506±3; 527±6	SHRIMP-zircon (cores)	This study
	Syn-tectonic leucogranite dike	520–32.0	SHRIMP-zircon (cores)	This study
Mabja (Sakya)	Deformed granite orthogneiss	530±9	SHRIMP-zircon	Lee and Whitehouse (2007)
	Migmatite	527±23	SHRIMP-zircon (cores)	Lee and Whitehouse (2007)
Mabja (Sakya)		35.0±0.8		
		(rims)		
Mabja (Sakya)	Migmatite	470±8	SHRIMP-zircon (cores)	Lee and Whitehouse (2007)
		22.5±0.6		
Mabja (Sakya)	Post-tectonic granite	16.2±0.4	SHRIMP-zircon	Lee and Whitehouse (2007)
	Syn-tectonic leucogranite dike	23.1±0.8	SHRIMP-zircon	Lee et al. (2006)
Malashan	Post-tectonic granite	14.2±0.2	SHRIMP-zircon	Lee et al. (2006)
	Post-tectonic granite	14.5±0.1	TIMS-monazite	Lee et al. (2006)
Malashan	Deformed granite	27.5±0.5	TIMS-zircon	Zhang et al. (2004)
	Post-tectonic granite	14.4±0.1	TIMS-zircon and monazite	Zhang et al. (2004)
Malashan	Post-tectonic granite	9.8±0.7	U-Pb-zircon	Schärer et al. (1986)
	Deformed granite orthogneiss	17.8±1.1	SHRIMP-zircon	Aoya et al. (2005)
Malashan	Weakly deformed granite	18.6±2.8	SHRIMP-zircon	Aoya et al. (2005)
	Weakly deformed granite	19.3±3.9	SHRIMP-zircon	Kawakami et al. (2007)

crustal channel (Beaumont et al., 2001, 2004; Hodges, 2006), and/or a combination of these processes, including thrusting over a mid-crustal ramp (Lee et al., 2000, 2006).

In this paper, we present new U-Pb SHRIMP spot ages from orthogneiss and leucogranite intrusions exposed in the core of the Kampa Dome. We combine these results with new structural and metamorphic data and previously published  $^{40}\text{Ar}/^{39}\text{Ar}$  thermochronology (Quigley et al., 2006) to reconstruct temperature-time and deformational histories for rocks within the Kampa Dome. Our results indicate that (1) the Kampa granite is a Cambrian pluton that was strongly deformed and metamorphosed at high temperatures ( $\sim 400\text{--}700^\circ\text{C}$ ) during Himalayan orogenesis, (2) the contact between the Kampa granite and overlying metasedimentary rocks is a high-strain zone that preserves evidence for episodes of top-to-N and top-to-S ductile shearing and later brittle deformation, and (3) structural, metamorphic and geochronologic datasets are consistent with, but not necessarily unique to, the surfacing of

a mid-crustal channel in the cores of the North Himalayan gneiss domes, as predicted by ‘channel flow extrusion’ models (Beaumont et al., 2001, 2004).

## 2. Geology of Kampa Dome

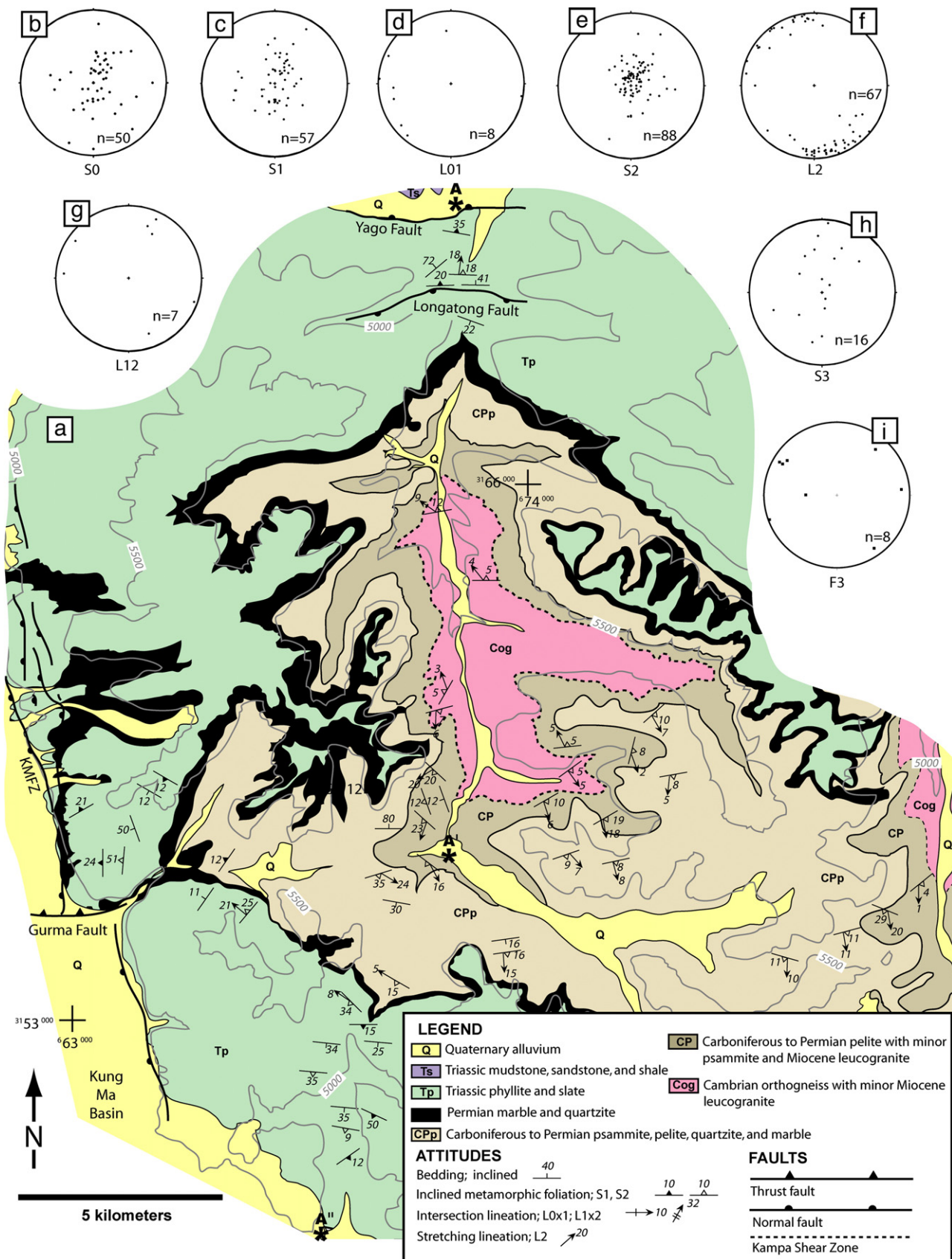
The Kampa Dome is situated between the well-studied Kangmar (Burg et al., 1984; Chen et al., 1990; Lee et al., 2000) and Mabja Domes (Zhang et al., 2004; Lee et al., 2004, 2006) along the North Himalayan antiform, roughly 40 km north of the South Tibetan Detachment System and 50 km south of the India–Asia suture (Indus–Tsangpo Suture Zone) (Fig. 1). Quigley et al. (2006) were the first to conduct detailed geologic investigations of the Kampa Dome. The dome outcrops as an E–W trending  $\sim 10\text{ km} \times 20\text{ km}$  ellipse, defined by a gently undulating contact between the domal core and the overlying cover sequence. The dome core consists of strongly deformed granitic orthogneiss (‘Kampa granite’; Quigley et al., 2006) containing the assemblage quartz+plagioclase+K-feldspar+biotite±muscovite±chlorite±epidote. The Kampa granite is overlain by Carboniferous to Jurassic sedimentary rocks including psammites, pelites, calc-schists and marbles (Fig. 2). Mineral assemblages in pelites indicate a progressive series of Barrovian-type metamorphic zones defined by chloritoid-in, garnet-in, staurolite-in and kyanite-in isograds (Fig. 3). Metamorphic zones are roughly concentric around the Kampa granite and increase in grade with increasing structural depth towards the granite contact, consistent with interpretations from the Kangmar (Burg et al., 1984; Chen et al., 1990; Lee et al., 2000), Mabja (Lee et al., 2006) and Malashan Domes (Aoya et al., 2006). Kyanite was observed only in the central part of the dome, suggesting that this part of the dome exposes deeper crustal levels or that the kyanite zone was tectonically removed or thermally overprinted in stratigraphically equivalent parts of the dome where it is absent. Both the Kampa granite and basal parts of the metasedimentary sequence are intruded by a series of deformed garnet+muscovite±biotite±tourmaline leucogranite dikes and sills (Fig. 4) (Quigley et al., 2006). The contact between the Kampa granite and metasedimentary rocks consists of strongly deformed granitic and metasedimentary rocks with evidence for ductile and brittle deformation (Quigley et al., 2006).

## 3. Structural geology

We documented two high-temperature, penetrative ductile deformational events ( $D_1$  and  $D_2$ ), one lower temperature, localized brittle–ductile deformational event ( $D_3$ ) and one low-temperature, localized brittle deformation event ( $D_4$ ) in the Kampa Dome (Quigley et al., 2006). The spatial–temporal distributions of each phase of deformation are outlined in Sections 3.1–3.4 and the relationships between deformation and metamorphism are discussed in Section 3.5.

### 3.1. $D_1$ deformation

$D_1$  structures are best exposed at the structurally highest levels in northern Kampa Dome, where Jurassic and Upper



Triassic strata are deformed by macro- to mesoscopic, typically disharmonic  $F_1$  folds with axial surfaces oriented roughly E–W. Near the village of Yago, WNW-striking, gently S-dipping, S-vergent nappes are refolded by NW- to SW-striking, upright, open folds with subhorizontal to gently W-plunging axes (Fig. 5). Both folds are classified as  $D_1$  structures because they are interpreted to record progressive ~N–S contractional deformation. At slightly deeper crustal levels, a fine-grained spaced cleavage ( $S_1$ ) is developed within Upper Triassic rocks (Fig. 5). This fabric becomes a strongly developed, coarser grained foliation defined by biotite and quartz in Lower Triassic rocks. A series of W-striking, gently N-dipping, open to tight recumbent  $F_1$  folds containing a consistent, strongly developed  $S_1$  axial planar foliation and associated subhorizontal  $S_0$ – $S_1$  intersection lineation (Fig. 2d) have developed at this level (Fig. 5d).  $S_0$ – $S_1$  relationships at the outcrop scale indicate local N-vergence, although it is likely that these folds are parasitic to a larger S-vergent recumbent structure given the dominance of S-vergent structures in this region (Ratschbacher et al., 1994). At deeper structural levels in the metasedimentary sequence,  $S_1$  is progressively transposed by more shallowly dipping  $D_2$  fabrics (Fig. 5) and is only preserved as inclusion trails in metamorphic porphyroblasts that are commonly oblique to the external matrix foliation. In summary,  $D_1$  structures preserved within the upper parts of Kampa Dome indicate ~N–S contractional deformation and related crustal thickening.

### 3.2. $D_2$ deformation

$S_2$  first appears in Triassic phyllites on the northern flank of Kampa Dome (Fig. 5) as a shallowly N-dipping spaced cleavage that cross-cuts  $S_1$  and contains a weakly developed, variably oriented  $L_{1,2}$  intersection lineation (Fig. 2g). The intensity of  $S_2$  increases dramatically with structural depth over roughly 20 m of vertical thickness to become a penetrative foliation with a shallowly NNW or SSE-plunging mineral lineation (Fig. 2f), defined by elongate mineral grains including biotite and amphibole (Quigley et al., 2006). On the south limb of the dome,  $S_2$  dips gently to the south and overprints steeper  $S_0$  and  $S_1$ .  $S_0$  +  $S_1$  fabrics display s-shaped sigmoidal patterns between spaced  $S_2$  cleavage planes, suggesting oblique lateral shortening relative to the  $S_0$ / $S_1$  fabric. At deeper levels  $S_2$  becomes an intensely developed mylonitic fabric that is commonly boundnaged along with the associated lithologic layering, indicating significant stretching parallel to  $L_2$  and shortening perpendicular to  $S_2$ . In the Kampa granite,  $S_2$  is a strongly developed, shallowly dipping foliation (Figs. 2, 5) defined by preferred orientations of micas and flattened, recrystallized ribbon quartz domains (Fig. 4c).  $S_2$  predominately dips gently to the north or south away from the core of the dome (Fig. 2) and contains a

strongly developed mineral lineation, defined by elongate quartz and feldspar grains and aggregates of finer-grained biotite with aspect ratios (length:width) up to 6:1.  $L_2$  plunges gently down-dip to the NNW or SSE (Fig. 2f). K-feldspar porphyroclasts and quartz boudins display shape geometries that indicate primarily top-to-N shear (with some symmetric and top-to-S shear indicators) in the direction of  $L_2$ . In thin sections of the Kampa granite, K-feldspar porphyroclasts are wrapped by  $S_2$ , commonly internally deformed (as indicated from undulatory extinction and deformation twins), strongly sericitized, and have abundant myrmekite growth along grain boundaries, suggesting deformation at temperatures of >400–500 °C (Tullis and Yund, 1991). Quartz grains range from unstrained, coarsely recrystallized grains to elongate grains with strongly developed ‘sweeping’ undulose extinction indicating deformation at both lower (300–400 °C) and higher (>400 °C) temperatures (Hirth and Tullis, 1992). Biotite grains are aligned in  $S_2$  and internally undeformed.

The increase in  $S_2$  intensity with depth led Quigley et al. (2006) to interpret the high-strain zone developed at the base of the metasedimentary sequence and top of the Kampa granite as a ductile shear zone (‘Kampa Shear Zone’). Shear sense indicators obtained from this zone indicate primarily top-to-N deformation cross-cut by localized top-to-S  $D_3$  deformation bands (Fig. 5). At one locality, quartz veins with asymmetric geometries indicate top-to-S shear sense (Fig. 4f). The fabric containing these veins is cross-cut by a leucogranite sill, with sheared upper and lower contacts indicated by foliation drag in the adjacent wall rock (Fig. 4d). We interpret the foliation drag to reflect top-to-N shear during of after leucogranite emplacement, suggesting a change in shearing polarity at this time. The data are consistent with either a regional change from top-to-S shear during  $D_1$  to top-to-N shear during  $D_2$  (Chen et al., 1990; Aoya et al., 2005, 2006) or a combination of top-to-N and top-to-S shearing events during  $D_2$  (Lee et al., 2000). Given the penetrative nature of  $D_2$  fabrics with depth, it appears most likely that the shear sense indicators observed at this locality record  $D_2$  deformation. In light of the cross-cutting relationships, we suggest that the Kampa Shear Zone records evidence for both top-to-S and top-to-N shearing during  $D_2$ . In at least one location, this deformation was associated with a change from top-to-S to top-to-N shearing during or after the emplacement of leucogranite sills.

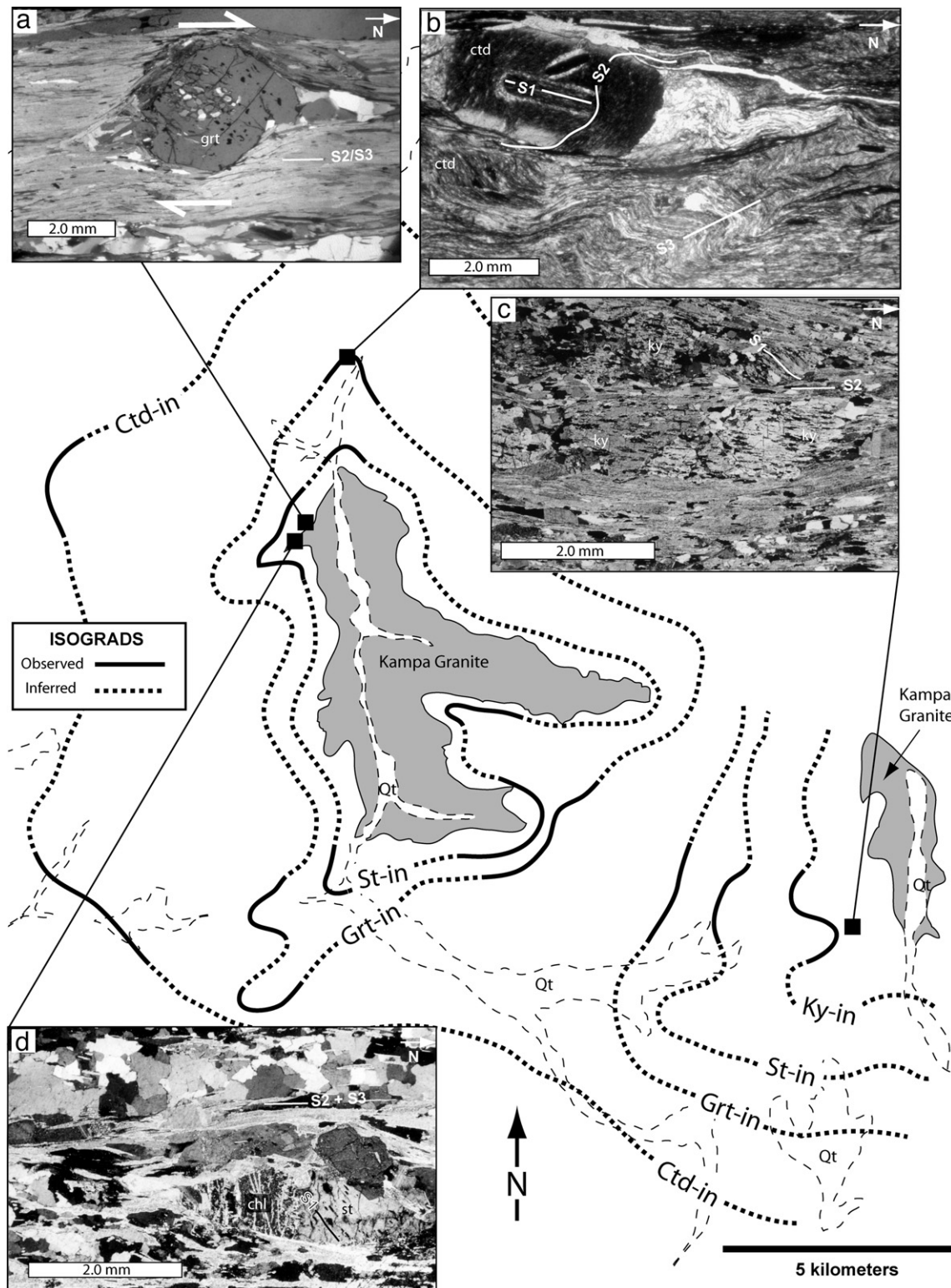
### 3.3. $D_3$ deformation

$D_3$  structures include (1) top-to-N shear zones parallel to  $S_2$  within the Kampa Shear Zone, (2) evenly spaced top-to-N brittle–ductile shear zones and faults distributed throughout the metasedimentary sequence on the northern limb of Kampa

Fig. 2. (a) Geological map of the western Kampa Dome showing major lithologic units, structural data and major brittle faults. Geologic contacts were identified and mapped along major valley systems, with observed contacts indicated by proximity to structural measurements. Geologic contacts were extrapolated into more remote regions of the dome using ASTER image interpretation. KMFZ=Kung Ma Fault Zone. Structural data plotted on lower hemisphere, equal area stereonet projections with the number of measurements indicated, (b) poles to bedding, (c) poles to  $S_1$  foliation and  $F_1$  axial surfaces, (d)  $L_{01}$  intersection lineations and  $F_1$  fold axes, (e) poles to  $S_2$  foliation and  $F_2$  axial planes, (f)  $L_2$  mineral lineations and  $F_2$  fold axes, (g)  $L_{12}$  intersection lineations, (h) poles to  $S_3$  foliation and  $F_3$  axial planes, (i)  $F_3$  fold axes. Location of Fig. 5 cross-section shown by A,  $A^I$ , and  $A^{II}$ .

Dome (Fig. 5a), (3) a spaced, anastomosing  $S_3$  crenulation cleavage within and adjacent to the  $D_3$  high-strain zones that cross-cuts  $S_2$  (Fig. 5c), and (4) localized top-to-S shear zones and development of E–W striking open folds and weakly developed axial planar fabrics on the southern limb of the dome. Where  $D_2$  and  $D_3$  fabrics are parallel,  $D_3$  deformation is recognized by

highly undulatory extinction and subgrain formation in quartz and undulatory extinction in feldspar, indicative of lower temperature deformation conditions ( $\sim 300$ – $400$  °C; Hirth and Tullis, 1991). Quartz veins within  $D_3$  shear zones have been deformed in both ductile (folding and boudinaging) and brittle (fracturing) fashion and display consistent top-to-N shear sense



indicators for both (Fig. 5a). In the thin section, quartz exhibits highly undulatory extinction and subgrain formation and micas are kink folded (Fig. 3b), have undulatory extinction (Quigley et al., 2006) and are locally retrogressed to chlorite, suggestive of low-grade (250–400 °C) deformation. Pseudotachylite veins are also present. The microstructures and associated metamorphic mineral assemblages suggest D<sub>3</sub> initiated at temperatures below D<sub>2</sub> and continued while rocks crossed the brittle–ductile transition.

On the south limb of the dome, small low-grade shear zones in the Kampa granite cross-cut S<sub>2</sub> and indicate top-to-S shearing (Fig. 5). Open folds of S<sub>2</sub> in the overlying metasedimentary rocks have ~E–W striking axial planes roughly perpendicular to the inferred transport direction from the D<sub>3</sub> shear zones. This suggests that these folds may have formed in localized zones of compression associated with D<sub>3</sub> shearing. If top-to-N D<sub>3</sub> structures on the north limb of the dome and top-to-S D<sub>3</sub> structures on the south limb of the dome formed synchronously, this suggests (but does not absolutely prove) that D<sub>3</sub> deformation was concurrent with crustal doming because D<sub>3</sub> structures indicate opposing, dome-outward sense of shear. In summary, D<sub>3</sub> structures preserved in Kampa Dome indicate top-to-N shearing and faulting on the north limb of Kampa Dome, localized top-to-S shearing and faulting on the south limb of Kampa Dome, and associated crustal thinning.

#### 3.4. D<sub>4</sub> brittle deformation

D<sub>4</sub> brittle structures in the Kampa Dome include (1) E–W striking normal faults, (2) NW–SE to E–W striking strike-slip faults; (3) N–S striking normal faults; and (4) an E–W striking thrust fault (Figs. 2, 6). E–W striking normal faults include N-dipping and S-dipping sets. N-dipping normal faults are the oldest preserved brittle structures and are most common on the N limb of the dome, where they cross-cut D<sub>3</sub> high-strain zones (Figs. 2, 5). The close spatial relationship and consistent kinematics of D<sub>3</sub> high-strain zones and N-dipping normal faults suggest they record parts of a continuous deformation regime. S-dipping normal faults cross-cut the N-dipping faults and are locally associated with en-echelon quartz vein arrays (Fig. 5e). The Longatong Fault (avg. strike/dip=101/58) is the most prominent of these structures and is dominated by dip-slip

slickenlines that indicate an average hanging wall transport direction relative to footwall of 182°. The hanging wall and footwall of the Longatong Fault consist of lithologically equivalent metasedimentary rocks, suggesting that the prominent scarp associated with this structure formed from ~100 m of top-to-S dip-slip displacement (Fig. 6a).

A series of N-striking, steeply W-dipping normal faults collectively composing the Kung Ma Fault Zone traverse the western margin of the Kampa Dome (Figs. 2, 6b). The average strike/dip of the faults is 171°/56°W. Fault planes are locally corrugated on the meter scale, resulting in local variations in orientation. They contain strongly developed dip-slip slickenlines with average trend/plunge of 276°/52°W (Fig. 6b), indicating westward motion of the hanging wall relative to the footwall. The Kung Ma Basin resides in the downthrown hanging wall and contains strongly deformed Late Pleistocene strata (Quigley, 2006).

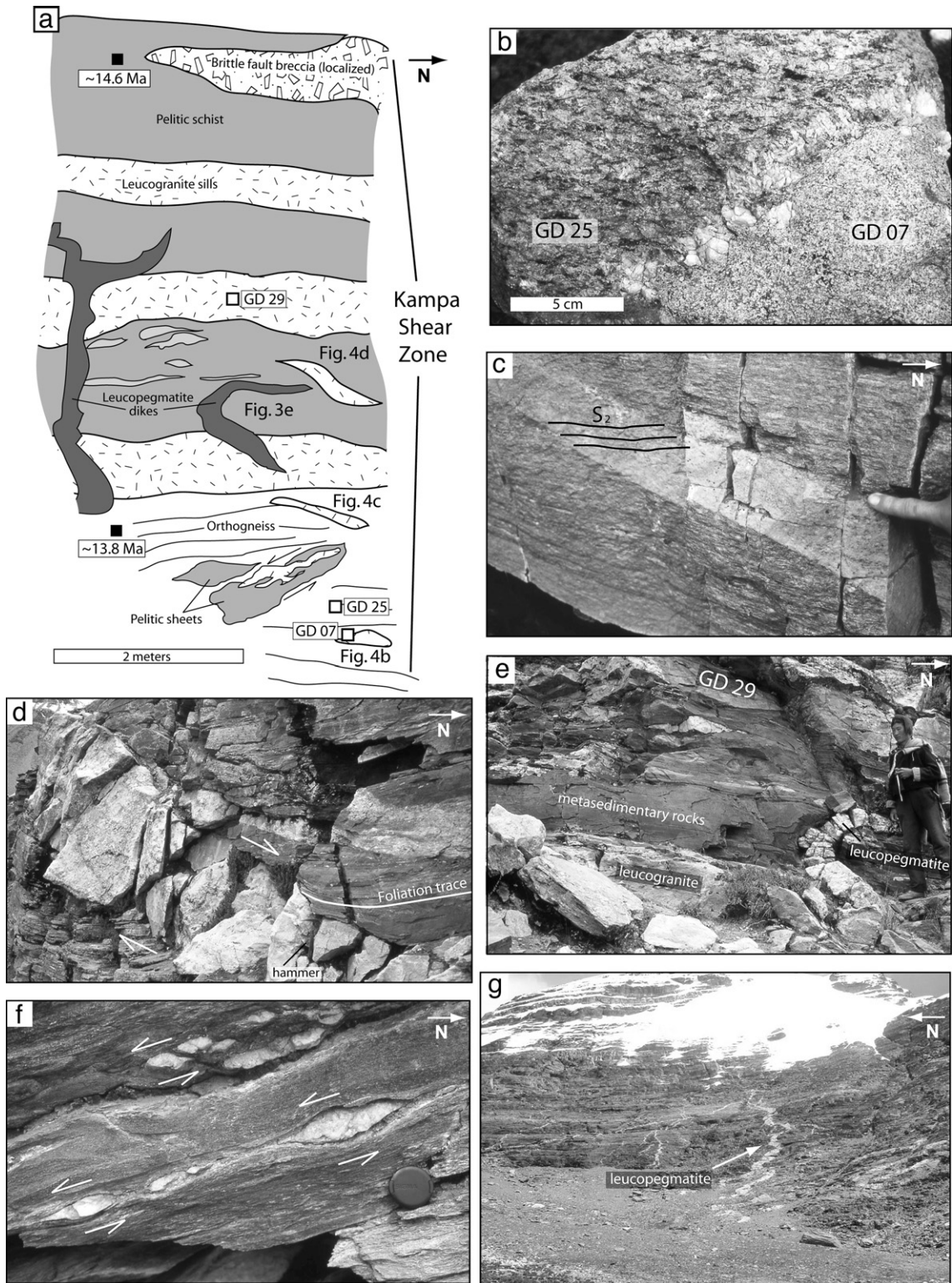
The surface trace of the Kung Ma Fault Zone takes an apparent right-lateral step in the SW corner of Kampa Dome (Fig. 2). At this location, a mid-slope rill channel exposes metasedimentary slate thrust southward over a footwall of loosely consolidated hillslope colluvium along the Gurma Fault (Fig. 6c). The fault strikes towards 282° and dips 26° north-northeast (Fig. 6b inset). No slickenlines were observed on the fault plane; however a major component of reverse slip is indicated by the relationship between older, overthrust Paleozoic bedrock and younger, underlying colluvium (Fig. 6c). The fault scarp has been buried by additional colluvium subsequent to the last displacement event. The trace of this thrust fault connects with a ~7 m high ridge developed in Quaternary alluvial deposits within the Kung Ma Basin, indicating youthful displacement (Fig. 6d) (Quigley, 2006). The extent to which the present ridge height reflects finite fault displacement is uncertain, given that the toe of the ridge has been eroded by a stream system exiting the ranges. However, the connectivity between the ridge and fault exposure suggests that ridge formed, at least in part, in response to tectonic uplift. The extent to which this fault continues to the east into the dome and its total displacement is unknown. Given the absence of an exposed relationship between the Gurma and Kung Ma Faults, it is unclear whether the former is simply an accommodation fault along the Kung Ma Fault Zone or whether it is a later fault that offsets the Kung Ma Fault.

**Fig. 3.** Spatial distribution of chloritoid-in (ctd-in) garnet-in (grt-in), staurolite-in (st-in) and kyanite-in (ky-in) metamorphic isograds in Kampa Dome. (a–d) Photomicrographs of pelitic schist units showing microstructural relationships between porphyroblast growth and fabric development. All thin sections cut parallel to L<sub>2</sub> stretching lineation and perpendicular to S<sub>2</sub>. (a) Garnet porphyroblast from the Kampa Shear Zone with oblique internal S<sub>1</sub> foliation wrapped by external composite S<sub>2</sub>+S<sub>3</sub> foliation. Asymmetric strain shadows of quartz+chlorite indicate top-to-N shearing following porphyroblast growth. Localized retrogression of garnet and mica in this sample indicate that deformation persisted into greenschist facies conditions associated with D<sub>3</sub> deformation and metamorphism. (b) Complex chloritoid porphyroblast–foliation relationships in lowermost Triassic schist unit. Large chloritoid containing sigmoidal S<sub>2</sub> fabric contains a smaller chloritoid with straight S<sub>1</sub> foliation. Samples at higher structural levels contain S<sub>1</sub> foliations defined by small chloritoids. Chloritoid growth thus occurred episodically from D<sub>1</sub> to late D<sub>2</sub>/early D<sub>3</sub> in this unit. The external S<sub>2</sub> foliation is strongly folded and a spaced S<sub>3</sub> crenulation cleavage has locally developed. Chloritoid within this particular sample has also undergone brittle fracturing and exhibits chloritization along grain boundaries and internal fractures, indicating that D<sub>3</sub> persisted under brittle–ductile conditions, (c) Kyanite porphyroblasts within the Kampa Shear Zone containing sigmoidal S<sub>1</sub> and straight S<sub>2</sub> foliations defined by mica and quartz inclusion trails. Mildly developed strain shadows within the sample indicate top-to-N shearing, implying that kyanite containing the presently inclined S<sub>1</sub> foliation was rotated clockwise and continued to grow during top-to-N D<sub>2</sub> shear. External S<sub>2</sub> foliation wraps porphyroblasts indicating that D<sub>2</sub> deformation persisted after kyanite growth ceased, (d) Staurolite porphyroblast from Kampa Shear Zone with oblique internal S<sub>1</sub> foliation wrapped by external composite S<sub>2</sub>+S<sub>3</sub> foliation. External foliation wraps staurolite and is locally associated with syn- and post-deformational chloritization of staurolite and biotite, indicating that retrograde metamorphism locally persisted beyond D<sub>3</sub> deformation. Left half of staurolite grain has been pseudomorphed by chlorite.

### 3.5. Relationships between deformation and metamorphism

Three phases of metamorphic mineral growth are evident based on textural relationships of metamorphic minerals with the D<sub>1</sub> to D<sub>3</sub> fabrics discussed above. Prograde metamorphism occurred during D<sub>1</sub> crustal thickening and is preserved pri-

marily within upper parts of the metasedimentary sequence. Peak metamorphism occurred during the early stages of D<sub>2</sub> and is preserved throughout the metasedimentary sequence. Retrograde metamorphism occurred during the late stages of D<sub>2</sub> and D<sub>3</sub> and is restricted to discrete deformation zones in the Kampa Shear Zone and overlying metasedimentary sequence.



In the upper parts of the metasedimentary sequence, chloritoid porphyroblasts are present both parallel and oblique to the  $S_1$  foliation and both include and are wrapped by  $S_1$ , indicating syn- $D_1$  porphyroblast growth. With increasing depth, the cores of chloritoid porphyroblasts contain  $S_1$  and the mantles contain  $S_2$ , indicating chloritoid growth occurred pre-to-syn  $D_2$  and possibly syn- $D_1$  (Fig. 3b). The  $S_1$  and  $S_2$  foliations overgrown by chloritoid consist of quartz+muscovite+chlorite±graphite±ilmenite, indicating chloritoid growth occurred during prograde metamorphism. Reconnaissance traverses through the southern part of Kampa Dome revealed similar structural and metamorphic relationships. At deeper crustal levels, garnet porphyroblasts are wrapped by  $S_2$  and contain straight  $S_1$  inclusion trails that are oriented at a high angle to the external foliation, suggesting garnet growth occurred late- to post- $D_1$  and pre- $D_2$ .

The progressive, down-section appearance of peak metamorphic porphyroblasts in pelitic assemblages including chloritoid, biotite, garnet (Fig. 3a), staurolite (Fig. 3d), and kyanite (Fig. 3c) delineate metamorphic isograds with a maximum metamorphic grade close to the basal contact with the Kampa granite (Fig. 3). Porphyroblasts contain either sigmoidal inclusion trails that are oblique to the external (matrix) foliation  $S_2$  or inclusion trails parallel to the external  $S_2$ . Collectively, these observations indicate porphyroblast growth occurred after the formation of  $S_1$  and during the development of  $S_2$ . All porphyroblasts are wrapped by matrix  $S_2$ , indicating  $D_2$  continued after peak metamorphism. On  $S_2$  planes, elongate metamorphic porphyroblasts such as hornblende and kyanite range from randomly oriented to strongly aligned parallel to  $L_2$ , further indicating syn- $D_2$  growth. Tension gashes oriented perpendicular to  $L_2$  stretching lineations occur in quartzofeldspathic lithologies and are infilled with amphibole.

The spatial distribution of retrograde metamorphism generally appears to coincide with  $D_3$  high-strain zones, where staurolite, garnet, biotite and chloritoid porphyroblasts are mantled and variably replaced by retrograde chlorite (Fig. 3d). Staurolite and garnet are also locally altered to biotite. Retrograde mineral growth is focused primarily along intra-grain fractures and in pressure shadows, indicating that retrograde metamorphism was accompanied by localized deformation under low-temperature ductile and brittle conditions. We suggest that retrograde metamorphism occurred during  $D_3$  as rocks were exhumed to shallower crustal levels. Kyanite crystals rimmed by andalusite are reported from Tethyan metasedimentary rocks elsewhere in the region, suggesting that localized retrograde metamorphism was associated with rapid uplift following Barrovian metamorphism (Burg et al., 1987).

#### 4. U/Pb geochronology

Zircon mineral separates were obtained from samples GD25 (Kampa granite), GD29 (leucogranite) and GD07 (leucogranite) using conventional heavy liquid and magnetic separation techniques. Analytical details appear in the Appendix. Both GD25 and GD29 contained a bimodal distribution of milky rounded grains ( $\sim 100 \mu\text{m}$ ) and euhedral grains ( $100\text{--}400 \mu\text{m}$ ). Single SHRIMP spot ages are quoted in the text with a precision of  $1\sigma$  (c. 68% confidence) whereas weighted mean ages are expressed in terms of a  $2\sigma$  uncertainty (c. 95% confidence).

Zircon grains recovered from all samples preserve dominantly euhedral to subhedral exteriors with aspect ratios of  $\sim 2.5:1$  and lengths of  $\sim 100\text{--}200 \mu\text{m}$ . CL images (Fig. 7a–e) show that the majority of euhedral grains exhibit oscillatory zoning, typical of igneous zircons. However, some euhedral grains were partly or totally metamict (Fig. 7c–e). Subhedral to anhedral grain fragments are either partly or totally metamict. 27 analyses on 23 zircons were obtained from the Kampa granite sample GD25 (Table 2, Fig. 7f,g). Of these, 21 analyses were of oscillatory zoned domains including cores and rims and 6 were of metamict grains. The metamict zircons have high U-contents (3999–13,153 ppm) and low to moderate Th/U ratios of 0.02–0.25. They record scattered and generally discordant mid-Phanerozoic  $^{206}\text{Pb}/^{238}\text{U}$  ages, ranging from 109 Ma to 283 Ma, as shown in Fig. 7g. In contrast, analyses from the cores and rims of oscillatory zoned grains have lower U-contents (140–3982 ppm) and a high average Th/U ratio of  $\sim 0.58$ . All of these, except spots 3.1, 4.1, 6.1, 11.1 and B5.1, have concordant  $^{206}\text{Pb}/^{238}\text{U}$  and  $^{208}\text{Pb}/^{232}\text{Th}$  ages (<5% discordance) and record exclusive Cambrian ages of 497–540 Ma. Moreover, they define two separate concordia age populations (Fig. 7f; after Ludwig, 1998) of  $506 \pm 3$  Ma (spots 1.2, 7.1, 8.1, 8.2, 9.1, 10.1B1.1 and B4.1) and  $527 \pm 6$  Ma (spots 2.1, 2.2, B2.1, B3.1 and B6.1). This could indicate that the Kampa granite incurred episodic zircon growth during protracted magmatism from 497 Ma to 540 Ma or that the granite contains older inherited zircons and was emplaced at ca. 506 Ma. The geologic significance of this heterogeneity is unclear. Spot B5.1, taken from a distinct dark core, has an older discordant  $^{206}\text{Pb}/^{238}\text{U}$  age of 719 Ma and this age is thought to reflect pre-magmatic inheritance. A tentative regression line (after York, 1969) forced through  $506 \pm 3$  Ma and including several of the younger discordant ages yields a lower intercept age of  $53 \pm 12$  Ma (Fig. 7g).

12 U–Pb zircon analyses were obtained for the leucogranite sample GD29 (Table 2, Fig. 7h), with 6 taken from metamict grains and 6 from those showing oscillatory zoning. At least three of the oscillatory zoned zircons (spots 2.1, 3.1 & 4.1)

Fig. 4. (a) Cross-section of the Kampa Shear Zone at the contact between the Kampa granite and overlying metasedimentary rocks. Location and age of biotite  $^{40}\text{Ar}/^{39}\text{Ar}$  samples shown, from Quigley et al. (2006). Location of field photos (b–g) and U–Pb geochronology samples as shown. (b) Sample displaying the contact between the Kampa granite (GD25) and garnet-bearing leucogranite (GD07). (c) Leucogranite sill with intrusive contact mildly oblique to  $S_2$  contains the  $S_2$  fabric internally, indicating syn- $D_2$  emplacement. (d) Leucogranite sill emplaced into pelitic schist. The middle of the sill is undeformed but it is sheared along its contact with the enveloping schist, which shows a change in foliation orientation that we interpret to reflect normal top-to-N foliation drag. Away from the leucogranite, the schist contains top-to-S shear sense indicators, indicating that intrusion of the leucogranite at this location was associated with a reversal in shear sense. (e) Location of GD29 deformed leucogranite sill sampled for U–Pb geochronology. The sills are cross-cut by a tightly folded pegmatitic leucogranite dike, indicating that  $D_2$  deformation persisted after their emplacement. (f) Deformed quartz boudins with asymmetric quartz strain shadows in the upper left and bottom right boudin corners, indicating top-to-S sense of shear. Asymmetry of the upper quartz boudin may be partially controlled by interference by adjacent boudins. (g) Deformed leucopegmatite dikes cross-cutting  $S_2$  in overlying metasedimentary rocks are folded with axial planes parallel to  $S_2$ , indicating syn- $D_2$  emplacement.

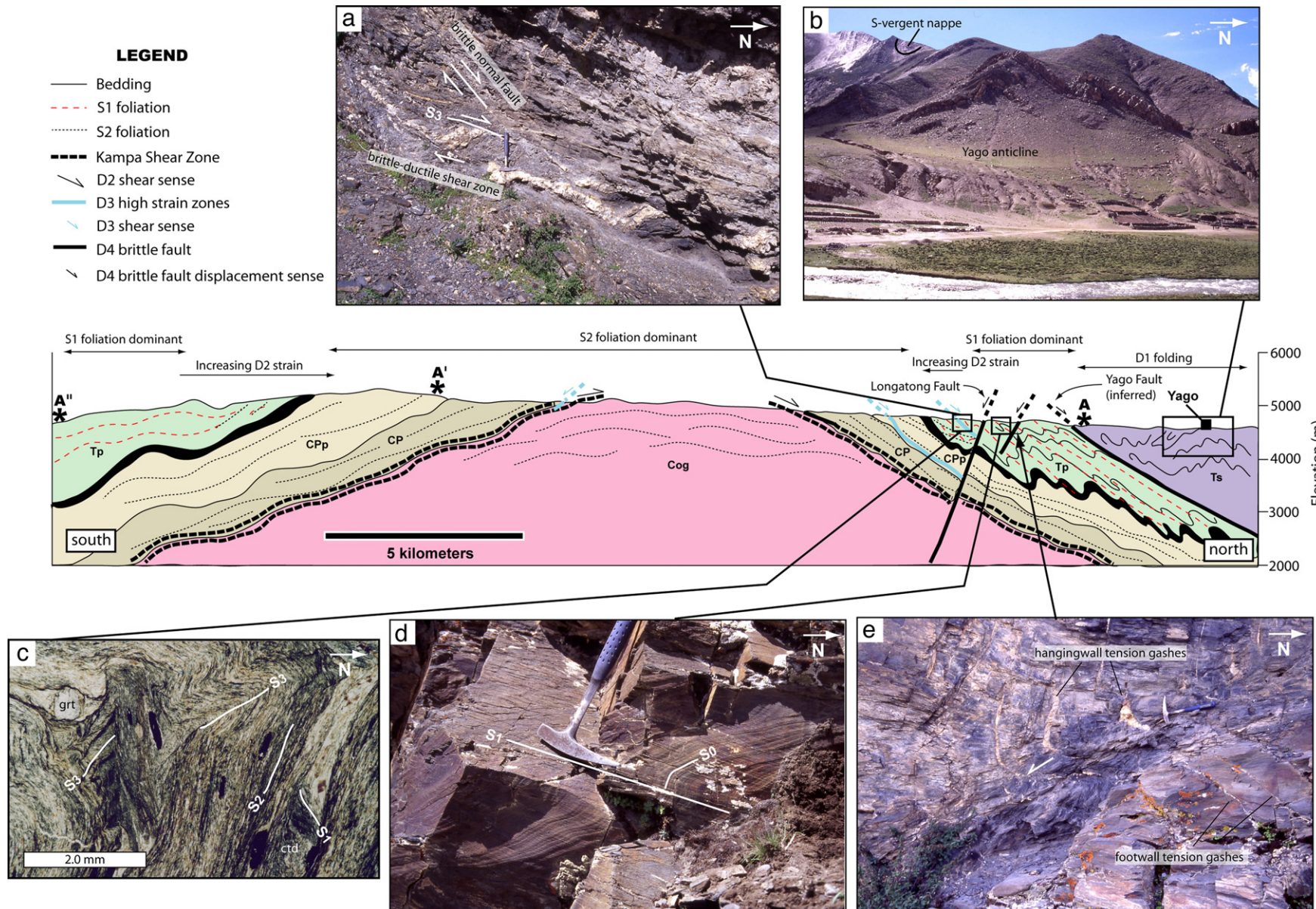


Fig. 5. Interpretive N–S geologic cross-section of the western Kampa Dome. See Fig. 2 for location of A, A<sup>I</sup>, and A<sup>II</sup> on section. (a) Gently N-dipping D<sub>3</sub> brittle–ductile high-strain zone with highly asymmetric sheared quartz veins indicating top-to-N movement. Shear zone is cross-cut by more steeply N-dipping D<sub>4</sub> normal faults. (b) Upright open F<sub>1</sub> folds of Jurassic sedimentary rocks near Yago. Earlier F<sub>1</sub> nappes are present in the limbs of the upright folds. (c) Photomicrograph showing textural relationships between S<sub>1</sub>, S<sub>2</sub>, and S<sub>3</sub> in grt-ctd-mica schist. S<sub>1</sub> is preserved as oblique inclusion trails in ctd porphyroblasts that are wrapped by external S<sub>2</sub> matrix foliation. S<sub>3</sub> is present as an axial planar crenulation cleavage in the hinges of F<sub>3</sub> folds of S<sub>2</sub>. (d) Development of spaced S<sub>1</sub> cleavage across bedding in the hinge of a recumbent F<sub>1</sub> fold of Upper Triassic phyllites. (e) Moderately S-dipping brittle normal fault with en-echelon hangingwall and footwall tension gashes filled with quartz.

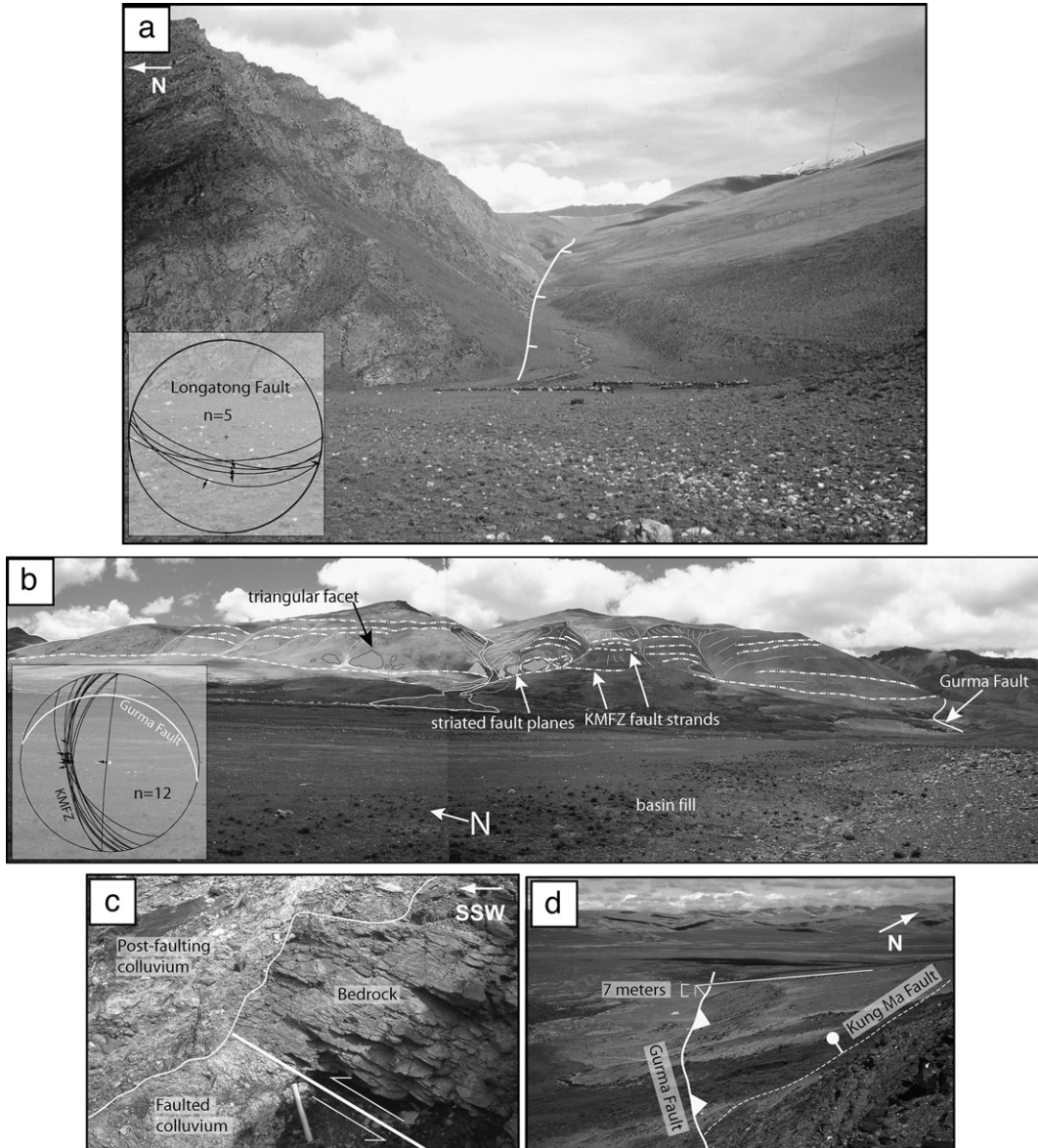


Fig. 6. Field photographs of  $D_4$  brittle faults and brittle fault structural data plotted on lower hemisphere, equal area stereonet projections with the number of measurements indicated (insets). (a) Photograph looking east along the strike of the Longatong Fault. Location of fault shown in Fig. 2. Hangingwall has been displaced at least 100 m down-to-the-south as indicated from the height of the footwall scarp. (b) Photograph of the Kung Ma Fault Zone (KMFZ) and Gurma Fault looking east across the Kung Ma Basin. Location of normal fault strands, striated fault planes and triangular faceted fault surfaces as indicated. Stereonet data indicates westward transport of hanging wall relative to footwall along the KMFZ. (c) The Gurma Fault exposure, revealing bedrock thrust southward over hillslope colluvium and draped by younger colluvium. (d) Westward continuation of the Gurma Fault as a ~7 m high ridge.

record concordant Cambrian  $^{206}\text{Pb}/^{238}\text{U}$  ages of 504–547 Ma in accord with results from analogous igneous-type grains of the Kampa granite. Metamict grains tend to show disrupted U–Th–Pb systematics and record discordant Paleozoic  $^{206}\text{Pb}/^{238}\text{U}$  ages of 491–259 Ma. Several of these analyses show reverse discordance, possibly caused by alteration of the zircons from external agents such as hydrothermal or metamorphic fluids, resulting in a net Pb\* gain relative to U (e.g. Mattinson et al., 1996). Only 5 zircon analyses were acquired from leucogranite sample GD07. Two euhedral and oscillatory zoned zircons yielded  $^{206}\text{Pb}/^{238}\text{U}$  ages of ca. 422 Ma and ca. 520 Ma, the second of which is discordant to both  $^{207}\text{Pb}/^{235}\text{U}$  and  $^{208}\text{Pb}/^{232}\text{Th}$  ages. Three

analyses from anhedral-to-subhedral metamict grains gave apparent  $^{206}\text{Pb}/^{238}\text{U}$  ages of 52–32 Ma.

Cambrian zircons recovered from the both of the leucogranite samples (GD07 and GD29) must be inherited because the leucogranites are clearly younger than the mid-Paleozoic metasedimentary rocks they intrude. These zircons are probably sourced from the Kampa granite, given the similarities in zircon size, morphology and U–Th–Pb composition amongst these intrusions. The significance of the ages derived from metamict grains is unknown. The youngest metamict zircon age of ca. 32 Ma is not dissimilar from the ca. 27.5 Ma U–Pb emplacement age obtained from a lithologically equivalent leucogranite body in

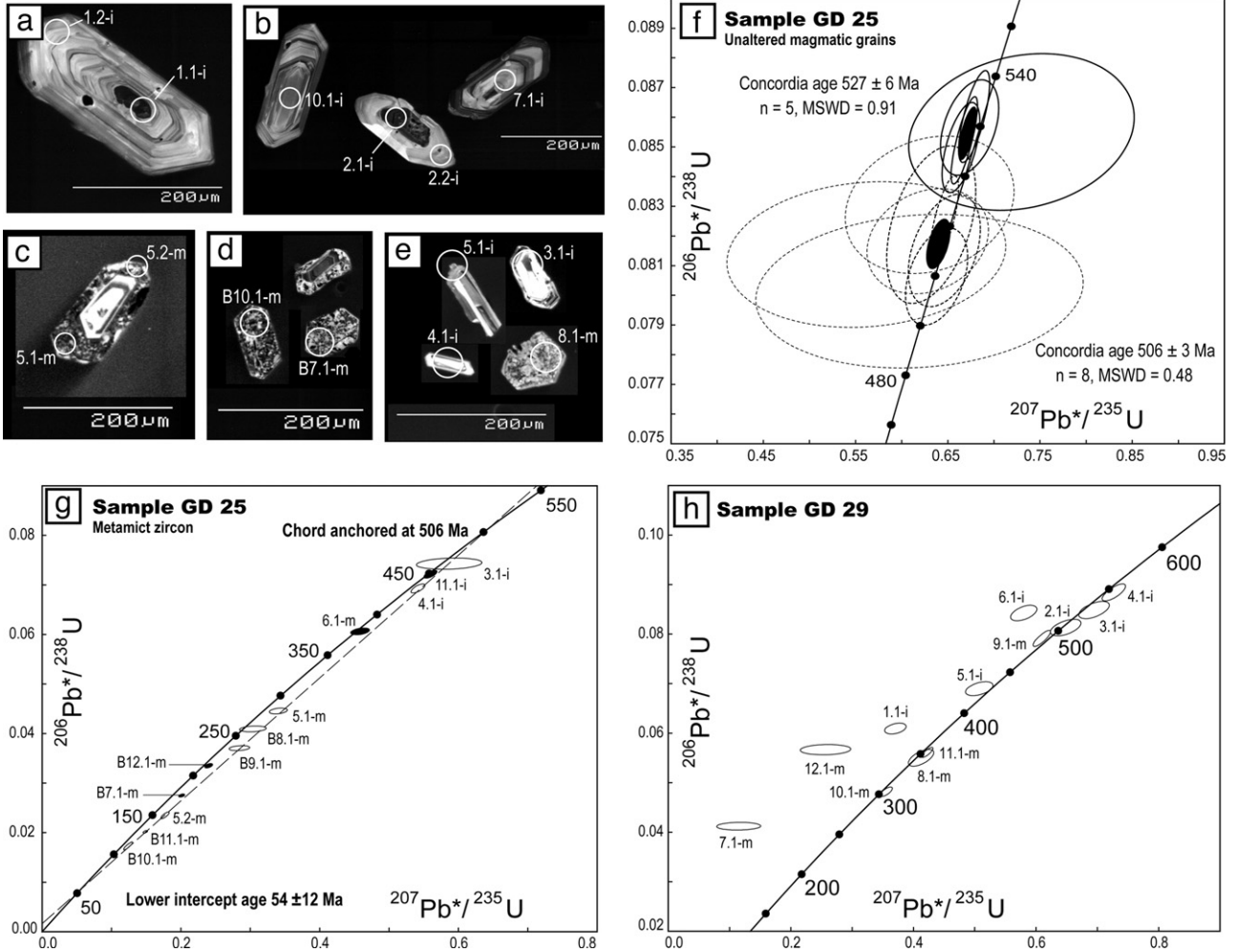


Fig. 7. (a)–(e) Cathodoluminescence images of selected zircons from GD25 (a–d) and GD29 (e), showing SHRIMP spot analysis number. Dark portions of zircons correspond to high uranium concentrations and patchy regions (c, d) indicate metamict zircon. Note that many metamict grains maintain euhedral forms despite internal alteration. (f)–(h) Standard Wetherill concordia plots for (f) magmatic zircon populations in GD25, (g) metamict zircons in GD25 and (h) zircons in GD29. Error ellipses are  $1\sigma$ .

the Mabja–Sakya Dome (Zhang et al., 2004). However, there is insufficient data to conclude that this is the intrusion age for the leucogranites in the Kampa Dome. We infer that the young metamict ages reflect Pb loss during Himalayan orogenesis and metamorphism. Zircon metamictization may occur at temperatures as low as  $\sim 500$ – $550$  °C in Barrovian terrains where rocks have been subjected to metamorphic fluid infiltration (Breeding et al., 2004).

## 5. Temperature–time–deformation history of Kampa Dome

We constructed a temperature–time–deformation path for Kampa Dome rocks (Fig. 8) by combining the U–Pb zircon, metamorphic and structural datasets (this study) with  $^{40}\text{Ar}/^{39}\text{Ar}$  mica thermochronology from Kampa Dome (Quigley et al., 2006) and regional geological relationships (Lee et al., 2000, 2004, 2006; Lee and Whitehouse, 2007). We applied several caveats in constructing this diagram. U–Pb analyses of zircon cores and rims from the Kampa granite are Cambrian in age and do not exhibit any evidence of younger growth, although some alteration is

indicated by partially metamict grains. No evidence for partial melting and/or migmatitization of the Kampa granite was observed at the present levels of exposure. These relationships suggest that Himalayan metamorphism of the Kampa granite did not exceed temperatures of  $\sim 700$  °C (e.g., Vavra et al., 1999; Rubatto et al., 2001; Lee and Whitehouse, 2007). Zircon metamictization may occur at temperatures as low as 500–550 °C (Breeding et al., 2004). We therefore bracket the peak metamorphic temperatures obtained within the Kampa granite to  $>500$ – $550$  °C and  $<700$  °C, consistent with peak syn-D<sub>2</sub> temperature estimates based on microstructural observations (Fig. 8).

Pelitic schists immediately overlying the Kampa granite contain kyanite+staurolite peak metamorphic assemblages. Although sillimanite was observed both within a contact metamorphic aureole and as part of Barrovian metamorphic sequence in Mabja Dome (Lee et al., 2004), no evidence for sillimanite growth was observed in Kampa Dome. We did not conduct thermobarometric studies in Kampa Dome, however equivalent kyanite+staurolite zone rocks from the Kangmar Dome yield peak temperature and pressure estimates of  $\sim 624$  °C and 860 MPa

Table 2  
SHRIMP U–Th–Pb isotopic data for Kampa Dome zircons, southern Tibet

Spot	U (ppm)	Th (ppm)	Th/U	$^{206}\text{Pb}^*$ (ppm)	$^{206}\text{Pb}_c$ %	$^{206}\text{Pb}^*/^{238}\text{U}$	$^{206}\text{Pb}^*/^{238}\text{U}$ Age (Ma) $\pm 1\sigma$	$^{206}\text{Pb}^*/^{238}\text{U}$ $\pm 1\sigma$ %	$^{207}\text{Pb}^*/^{206}\text{Pb}^*$ $\pm 1\sigma$ %	$^{207}\text{Pb}^*/^{235}\text{U}$ $\pm 1\sigma$ %	$^{208}\text{Pb}^*/^{232}\text{Th}$ $\pm 1\sigma$ %
<i>Sample GD 07</i>											
1.1	241	104	0.45	1.0	14.10	422 $\pm$ 6	0.0674 $\pm$ 1.5	0.0579 $\pm$ 7.6	0.5381 $\pm$ 7.7	0.0200 $\pm$ 8.5	
2.1	117	70	0.62	2.9	8.60	520 $\pm$ 9	0.0827 $\pm$ 1.8	0.0481 $\pm$ 17.4	0.5488 $\pm$ 17.5	0.0223 $\pm$ 11.3	
3.1	15896	2359	0.15	0.2	124.83	52 $\pm$ 1	0.0091 $\pm$ 1.2	0.0472 $\pm$ 1.2	0.0594 $\pm$ 1.7	0.0157 $\pm$ 2.0	
4.1	11139	7357	0.68	43.3	123.72	45 $\pm$ 5	0.0073 $\pm$ 4.9	- $\pm$ -	- $\pm$ -	0.0045 $\pm$ 33.5	
5.1	7294	251	0.04	1.3	31.58	32 $\pm$ 0	0.0050 $\pm$ 1.4	0.0438 $\pm$ 6.7	0.0300 $\pm$ 6.9	- $\pm$ -	
<i>Sample GD 25</i>											
1.1-i	1825	725	0.41	137.3	0.29	540 $\pm$ 4	0.0873 $\pm$ 0.7	0.0561 $\pm$ 0.8	0.6755 $\pm$ 1.1	0.0278 $\pm$ 1.3	
1.2-i	140	107	0.78	10.1	1.04	514 $\pm$ 7	0.0829 $\pm$ 1.1	0.0537 $\pm$ 3.2	0.6141 $\pm$ 3.4	0.0260 $\pm$ 4.6	
2.1-i,r	2751	1126	0.42	203.4	0.11	532 $\pm$ 4	0.0860 $\pm$ 0.7	0.0570 $\pm$ 0.6	0.6761 $\pm$ 0.9	0.0267 $\pm$ 1.1	
2.2-i	153	124	0.84	11.4	1.58	526 $\pm$ 7	0.0850 $\pm$ 1.2	0.0566 $\pm$ 4.0	0.6640 $\pm$ 4.1	0.0275 $\pm$ 4.2	
3.1-i	280	232	0.86	18.0	3.22	450 $\pm$ 5	0.0723 $\pm$ 1.0	0.0352 $\pm$ 10.1	0.3510 $\pm$ 10.1	0.0268 $\pm$ 2.7	
4.1-i	3539	228	0.07	210.2	0.46	429 $\pm$ 4	0.0688 $\pm$ 0.9	0.0539 $\pm$ 1.1	0.5116 $\pm$ 1.4	0.0285 $\pm$ 3.6	
5.1-m,r	8665	1846	0.22	333.0	-0.28	283 $\pm$ 3	0.0449 $\pm$ 0.9	0.0643 $\pm$ 0.7	0.3980 $\pm$ 1.1	0.0097 $\pm$ 6.9	
5.2-m,r	7685	1778	0.24	153.9	0.79	147 $\pm$ 3	0.0231 $\pm$ 1.9	0.0491 $\pm$ 1.9	0.1567 $\pm$ 2.7	0.0086 $\pm$ 4.5	
6.1-r	4235	680	0.17	220.5	1.81	373 $\pm$ 3	0.0595 $\pm$ 0.8	0.0406 $\pm$ 4.8	0.3334 $\pm$ 4.8	0.0303 $\pm$ 2.7	
7.1-i	766	538	0.73	53.7	0.20	505 $\pm$ 5	0.0815 $\pm$ 0.9	0.0580 $\pm$ 1.1	0.6511 $\pm$ 1.5	0.0252 $\pm$ 1.9	
8.1-i	193	152	0.81	13.6	1.99	497 $\pm$ 6	0.0801 $\pm$ 1.1	0.0546 $\pm$ 4.6	0.6032 $\pm$ 4.7	0.0250 $\pm$ 6.3	
8.2-i,r	3406	1718	0.52	241.7	-0.21	513 $\pm$ 4	0.0828 $\pm$ 0.7	0.0596 $\pm$ 0.6	0.6800 $\pm$ 0.9	0.0247 $\pm$ 1.0	
9.1-i	160	191	1.24	11.4	1.05	509 $\pm$ 7	0.0821 $\pm$ 1.1	0.0576 $\pm$ 3.0	0.6520 $\pm$ 3.2	0.0242 $\pm$ 3.8	
10.1-i	597	229	0.40	42.4	0.19	511 $\pm$ 7	0.0826 $\pm$ 1.3	0.0582 $\pm$ 1.3	0.6628 $\pm$ 3.1	0.0243 $\pm$ 3.5	
11.1-i	2979	737	0.26	184.5	1.01	444 $\pm$ 3	0.0714 $\pm$ 0.7	0.0482 $\pm$ 2.2	0.4738 $\pm$ 1.9	0.0275 $\pm$ 1.4	
B1.1-i	560	422	0.78	38.9	-0.22	502 $\pm$ 5	0.0810 $\pm$ 0.8	0.0620 $\pm$ 1.1	0.6922 $\pm$ 1.4	0.0240 $\pm$ 1.7	
B2.1-i	1925	780	0.42	140.6	0.16	525 $\pm$ 4	0.0849 $\pm$ 0.7	0.0564 $\pm$ 0.9	0.6600 $\pm$ 1.1	0.0265 $\pm$ 1.2	
B3.1-i	1014	648	0.66	74.8	0.48	528 $\pm$ 4	0.0854 $\pm$ 0.8	0.0550 $\pm$ 1.3	0.6479 $\pm$ 1.5	0.0271 $\pm$ 1.5	
B4.1-i	533	412	0.80	37.8	0.98	506 $\pm$ 5	0.0817 $\pm$ 0.9	0.0544 $\pm$ 2.3	0.6131 $\pm$ 2.5	0.0256 $\pm$ 2.7	
B5.1-i,c	819	385	0.49	83.4	-1.10	730 $\pm$ 6	0.1199 $\pm$ 0.8	0.0827 $\pm$ 1.5	1.3678 $\pm$ 1.7	0.0286 $\pm$ 3.4	
B6.1-i	3982	1655	0.43	291.5	0.17	526 $\pm$ 4	0.0851 $\pm$ 0.7	0.0558 $\pm$ 0.6	0.6545 $\pm$ 0.9	0.0269 $\pm$ 1.0	
B7.1-m	6845	726	0.11	161.5	0.69	174 $\pm$ 1	0.0273 $\pm$ 0.7	0.0487 $\pm$ 1.6	0.1832 $\pm$ 1.7	0.0106 $\pm$ 3.8	
B8.1-m	3999	503	0.13	142.1	0.84	259 $\pm$ 3	0.0410 $\pm$ 1.0	0.0585 $\pm$ 1.7	0.3311 $\pm$ 2.0	0.0091 $\pm$ 14.5	
B9.1-m	4377	690	0.16	140.2	0.92	234 $\pm$ 2	0.0369 $\pm$ 0.8	0.0576 $\pm$ 1.8	0.2934 $\pm$ 2.0	0.0101 $\pm$ 8.0	
B10.1-m	13153	1645	0.13	194.3	1.06	109 $\pm$ 3	0.0170 $\pm$ 3.0	0.0445 $\pm$ 2.7	0.1044 $\pm$ 4.0	0.0077 $\pm$ 5.8	
B11.1-m	10151	2428	0.25	174.8	0.16	128 $\pm$ 1	0.0200 $\pm$ 0.7	0.0542 $\pm$ 1.0	0.1496 $\pm$ 1.3	0.0063 $\pm$ 2.0	
B12.1-m	4638	82	0.02	133.2	0.20	212 $\pm$ 2	0.0334 $\pm$ 0.8	0.0517 $\pm$ 0.9	0.2380 $\pm$ 1.2	0.0094 $\pm$ 29.0	
<i>Sample GD 29</i>											
1.1-i	1681	636	0.39	84.4	0.73	354 $\pm$ 5	0.0565 $\pm$ 1.2	0.0327 $\pm$ 10.7	0.25 $\pm$ 10.7	0.0257 $\pm$ 2.5	
2.1-i	279	248	0.92	19.6	1.13	504 $\pm$ 8	0.0814 $\pm$ 1.4	0.0578 $\pm$ 2.1	0.65 $\pm$ 2.5	0.0162 $\pm$ 4.2	
3.1-i	251	235	0.97	18.4	1.12	526 $\pm$ 8	0.0850 $\pm$ 1.4	0.0594 $\pm$ 2.0	0.70 $\pm$ 2.4	0.0178 $\pm$ 3.2	
4.1-i	699	585	0.87	53.1	0.40	547 $\pm$ 8	0.0885 $\pm$ 1.3	0.0596 $\pm$ 1.2	0.73 $\pm$ 1.7	0.0200 $\pm$ 2.0	
5.1-i	1366	522	0.39	81.7	0.52	430 $\pm$ 6	0.0689 $\pm$ 1.3	0.0533 $\pm$ 2.6	0.51 $\pm$ 2.9	0.0239 $\pm$ 4.2	
6.1-i	1692	2128	1.30	123.8	0.30	522 $\pm$ 8	0.0843 $\pm$ 1.2	0.0498 $\pm$ 2.1	0.58 $\pm$ 2.4	0.0250 $\pm$ 3.2	
7.1-m	1786	573	0.33	65.5	0.33	259 $\pm$ 4	0.0409 $\pm$ 1.2	0.0199 $\pm$ 21.3	0.11 $\pm$ 21.3	0.0265 $\pm$ 1.8	
8.1-m	3919	556	0.15	187.3	1.01	344 $\pm$ 7	0.0549 $\pm$ 2.1	0.0544 $\pm$ 2.6	0.41 $\pm$ 3.3	0.0233 $\pm$ 3.1	
9.1-m	7807	11385	1.51	532.0	0.35	491 $\pm$ 8	0.0791 $\pm$ 1.3	0.0559 $\pm$ 0.9	0.61 $\pm$ 1.6	0.0271 $\pm$ 1.4	
10.1-m	1864	323	0.18	77.1	0.24	302 $\pm$ 4	0.0479 $\pm$ 1.3	0.0537 $\pm$ 1.3	0.36 $\pm$ 1.8	0.0228 $\pm$ 2.5	
11.1-m	4842	3049	0.65	233.7	0.17	351 $\pm$ 5	0.0560 $\pm$ 1.2	0.0547 $\pm$ 0.9	0.42 $\pm$ 1.5	0.0198 $\pm$ 12.6	
12.1-m	12372	17789	1.49	654.6	0.10	381 $\pm$ 6	0.0608 $\pm$ 1.2	0.0440 $\pm$ 2.9	0.37 $\pm$ 3.1	0.0245 $\pm$ 1.6	

i=magmatic (igneous-type) zircon, m=metamict zircon, c=core, r=rim. Pb<sub>c</sub> and Pb\* indicate the common and radiogenic portions of Pb respectively. Common Pb corrected by assuming  $^{206}\text{Pb}^*/^{238}\text{U}$ – $^{208}\text{Pb}^*/^{232}\text{Th}$  age-concordance. 1 $\sigma$  error in standard calibration was 0.57% for samples GD 07, GD 25 (spots B1.1–12.1) and GD 29; 0.41% for sample GD 25 spots 1.1–11.1 (not included in errors shown).

(Lee et al., 2000). Garnet-zone rocks from Kangmar yield peak temperature and pressure estimates of  $\sim$ 446 °C and 370 MPa (Lee et al., 2000). Dramatic crustal thinning following peak metamorphism is required in order to explain the telescoped isobars and isotherms relative to ‘expected’ continental gradients (e.g., Lee et al., 2000, 2004). Lee et al. (2000) concluded that the metasedimentary sequence at Kangmar was thinned to  $\sim$ 20% of its original thickness following peak metamorphism. Given the

similar map distribution of closely spaced isograds in Kampa Dome (Fig. 3), we suspect that a similar magnitude of vertical shortening occurred here. A large magnitude of D<sub>2</sub> crustal thinning is consistent with our observations that porphyroblasts are wrapped by S<sub>2</sub>, indicating significant vertical shortening followed peak metamorphism.

The timing of D<sub>1</sub> is unconstrained in Kampa Dome however a minimum age of D<sub>1</sub> can be obtained from maximum regional age

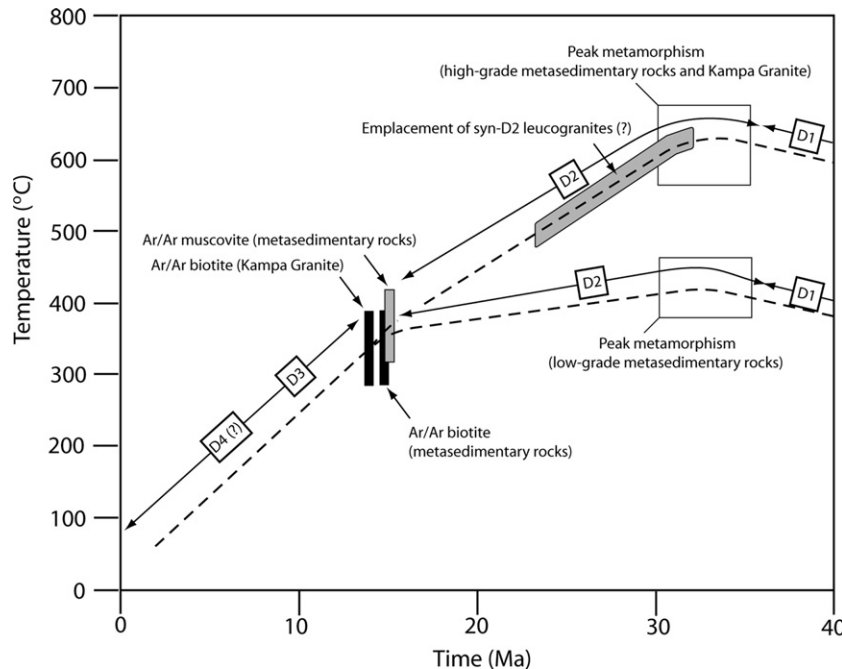


Fig. 8. Temperature–time plot showing inferred cooling histories for the Kampa granite and high-grade metamorphic rocks and low-grade metamorphic rocks based on geochronologic and thermochronologic data (Lee et al., 2000, 2004, 2006; Quigley et al., 2006; Lee and Whitehouse, 2007). Approximate timing of D<sub>1</sub> to D<sub>4</sub>, peak metamorphism, and leucogranite emplacement inferred from geologic relationships in Kampa Dome and other NHGD (see text). White boxes denote approximate temperature and age range of peak metamorphism indicated by syn-D<sub>2</sub> metamorphic assemblages.

constraints on D<sub>2</sub>, which clearly post-dates D<sub>1</sub>. On the basis of U/Pb zircon ages and geological relationships in syn-D<sub>2</sub> intrusions, Lee and Whitehouse (2007) concluded that D<sub>2</sub> deformation in Mabja Dome initiated at ~35 Ma, was ongoing at ~23 Ma, and had ceased by ~16 Ma. D<sub>2</sub> in Kangmar Dome is broadly constrained to between 40–20 Ma and ~15 Ma (Lee et al., 2000). We therefore suggest that D<sub>1</sub> initiated sometime prior to 40–20 Ma and probably after the onset of India–Asia collision between ~55 Ma (e.g., Klootwijk et al., 1992) and ~34 Ma (Aitchison et al., 2007)(Fig. 8).

On the basis of <sup>40</sup>Ar/<sup>39</sup>Ar mica thermochronology, Quigley et al. (2006) concluded that the metasedimentary sequence in Kampa Dome cooled rapidly through temperatures between 420 °C (upper closure temperature for muscovite) and 285 °C (lower closure temperature for biotite) by ~14.6 Ma and the Kampa granite cooled through temperatures between 385 °C and 285 °C by 13.7 Ma. The rapid cooling of the entire metasedimentary sequence at Kampa suggests that telescoping of the metamorphic sequence occurred during D<sub>2</sub> and that D<sub>2</sub> had ceased by ~14.6 Ma, generally consistent with temporal constraints from the Kangmar, Mabja, and Malashan Domes (Lee et al., 2000, 2006; Kawakami et al., 2007). Quigley et al. (2006) also suggested that mica cooling isotherms were domed after 13.7 Ma during D<sub>3</sub> transitional ductile-to-brittle deformation. We therefore infer that the timing of D<sub>2</sub> in Kampa Dome is constrained to between 40–20 Ma and ~14.6 Ma, and the timing of D<sub>3</sub> is constrained to younger than ~14.6 to 13.7 Ma. If linear, steady-state geotherms of 30–40 °C/km are assumed, exhumation of Kampa Dome rocks to the surface following mica cooling occurred at linear rates of ~0.5–0.9 mm/yr. On the basis of <sup>40</sup>Ar/<sup>39</sup>Ar and apatite fission track ages, Lee et al.

(2000) concluded that doming occurred in Kangmar Dome by ~11 Ma and that the dome cooled symmetrically from ~300° to 120 °C between ~11 and 5.5 Ma. In the absence of equivalent data from Kampa Dome, we extrapolated these temporal constraints in order to construct the *T*–*t*–*d* plot (Fig. 8).

## 6. Discussion

The structural and geochronologic data presented above shows that the granitic gneiss exposed in the core of Kampa Dome is a Cambrian pluton that was strongly deformed and metamorphosed during Himalayan orogenesis. Peak temperatures in the core of the dome during Himalayan metamorphism were <650–700 °C, indicated by Barrovian kyanite + staurolite assemblages in the immediately overlying metasedimentary rocks and an absence of migmatization and new zircon growth within the Kampa granite. Our interpretations are consistent with age estimates for granite gneiss coring the adjacent Kangmar Dome (Schärer et al., 1986; Lee et al., 2000). The absence of Himalayan zircon ages, the absence of sillimanite, and thermobarometric evidence for significant paleo-pressure differences between presently juxtaposed metasedimentary sequences led Lee et al. (2000) to conclude that the granite gneiss in Kangmar was not the heat source for Barrovian metamorphism. Conversely, the presence of Miocene zircon growth within the Malashan granite gneiss and the increase in metamorphic grade towards Miocene intrusions led Aoya et al. (2006) and Kawakami et al. (2007) to conclude that the granite gneiss in Malashan Dome intruded during Himalayan orogenesis, resulting in contact metamorphism in the overlying metasedimentary rocks. Since Himalayan zircon growth did not occur in the

Kampa granite, we prefer the interpretation that the present distribution of peak metamorphic assemblages within the Kampa metasedimentary sequence reflects structural thinning of a regional Barrovian metamorphic sequence (e.g., Lee et al., 2000). However, we cannot dismiss the possibility that thermal pulses related to Himalayan magmatism and fluid flow at or below present exposure levels may have influenced some of the metamorphic patterns observed in Kampa Dome, such as the partial replacement of kyanite, staurolite, garnet and chloritoid by retrograde biotite and chlorite within the Kampa metasedimentary sequence.

Several lines of evidence suggest that the contact zone between the Kampa granite and overlying metasedimentary rocks is a high-strain zone of regional significance. D<sub>2</sub> strain fabrics increase in intensity with depth towards this zone, where they become strongly foliated, lineated, and in places mylonitic. In addition, structural observations indicate the presence of both top-to-N and top-to-S shear sense indicators within this zone. Although it is permissible that these features formed synchronously, in at least one well documented locality in Kampa Dome a change from top-to-S to top-to-N shearing occurred during emplacement of leucogranite dikes, indicating a change in shearing polarity during (or possibly before) D<sub>2</sub> (Fig. 4). Similar combinations of top-to-S and top-to-N shear sense indicators have been recognized both within the South Tibetan detachment system (Hodges et al., 1996) and in other NHGD, where they have been identified as D<sub>1</sub> and D<sub>2</sub> structures, respectively (Chen et al., 1990; Aoya et al., 2005). We interpret this to indicate a major change in deformation kinematics during Himalayan orogenesis, and adopt the hypothesis of previous workers to suggest that the high-strain zone outcropping within the NHGD is regional in extent and correlates with the South Tibetan detachment (Chen et al., 1990; Lee et al., 2000). Although D<sub>2</sub> and D<sub>3</sub> structures preserved within Kampa Dome can be explained by south-ward extrusion of a mid-crustal channel from beneath a colder, more rigid medium (e.g., Grujic et al., 1996; Nelson et al., 1996), possibly linked to surface denudation along the Himalayan range front (Beaumont et al., 2001, 2004), these structures are also consistent with extrusion in response to gravity-driven collapse (Burchfiel and Royden, 1985; Burchfiel et al., 1992). Consequently, our data support both ‘channel flow’ and gravitational collapse models, but do not provide an independent means of distinguishing between these models.

Microstructures and associated metamorphic assemblages indicate continuous deformation within the Kampa shear zone during retrograde metamorphism, with partitioning of deformation into discrete top-to-N shear zones at lower temperatures. Parts of this zone and overlying fault zones also contain evidence for brittle faulting associated with N–S extension. Quigley et al. (2006) documented ~0.8 m.y. discordance in biotite  $^{40}\text{Ar}/^{39}\text{Ar}$  cooling age across the granite-metasedimentary rock contact, and hypothesized that this discordance resulted from structural omission of section within the Kampa shear zone following mica cooling. We interpret the contact between the Kampa granite and overlying metasedimentary rocks as an unconformity because (1) granite pebbles of similar composition to the Kampa granite are locally present in parts of

the metasedimentary sequence (Quigley et al., 2006) and (2) the Kampa granite is of Cambrian age while the immediately overlying metasedimentary rocks are Paleozoic. Given the intense D<sub>2</sub> fabrics and brittle faults observed at the granite-metasedimentary rock contact, it is clear that this unconformity was significantly modified by ductile and brittle deformation during Himalayan orogenesis.

The Barrovian metamorphism recorded in Kampa Dome has been identified in all other NHGD and in the Greater Himalayan Sequence (e.g., Hodges, 2000). The extent to the concentric arrangement of Barrovian metamorphic assemblages around the domal cores reflects thermal relaxation following crustal thickening (Lee et al., 2000, 2004; Quigley et al., 2006) and/or Himalayan granite emplacement (Aoya et al., 2005; Kawakami et al., 2007) may vary throughout the region. For the reasons stated above, we favor the hypothesis that the Kampa granite is a Cambrian pluton that was reworked under regionally elevated pressure and temperature conditions, as opposed to a Himalayan intrusion that was emplaced into a cooler sedimentary sequence, and therefore infer that the spatial and temporal distribution of metamorphism in Kampa Dome reflects regional (as opposed to contact) metamorphism.

Several aspects of the NHGD differ along the strike of the North Himalayan antiform, including (1) the distribution of Himalayan migmatites, syn-tectonic leucogranite intrusions, and post-tectonic granites, (2) the spatial distribution of post-Barrovian metamorphism, and (3) their map geometries. The volume of Himalayan intrusions exposed within the NHGD generally increases from east to west between Kangmar and Mabja (Watts et al., 2005), implying that western domes such as Mabja may expose deeper crustal levels than eastern domes such as Kampa and Kangmar (Lee et al., 2006). Variations in exposure depth also account for variations in the distribution of post-Barrovian metamorphism, as several of the Himalayan intrusions are associated with contact aureole that are not observed at Kampa Dome (Lee et al., 2006; Kawakami et al., 2007). The extent to which the retrograde D<sub>3</sub> fault zones we identified in Kampa occur in the other NHGD is unknown.

Lee et al. (2000) proposed that the NHGD were exhumed by thrusting over a north-dipping crustal ramp. Variations in NHGD map geometries, which range from elongate N–S (Kangmar), to elongate E–W (Kampa), to asymmetric (Mabja), might thus reflect changes in the shape and size of the footwall over which the NHGD were thrust (Lee et al., 2006). We hypothesize that dome geometries may also reflect along-strike variations in Miocene to Recent tectonism, as domes such as Kampa and Mabja are associated with major N–S striking normal faults and related extensional basins (Quigley, 2006) while others such as Kangmar are not.

## 7. Conclusions

New U/Pb ages from the Kampa Dome indicate that the Kampa granite is a Cambrian pluton that was strongly deformed and metamorphosed during Himalayan orogenesis. The contact between the Kampa granite and overlying metasedimentary rocks is a high-strain zone that, at least in one well documented

location, preserves evidence for top-to-S ( $D_1$  or  $D_2$ ) followed by top-to-N ( $D_2$ ) ductile shearing. This deformation zone also contains evidence for retrograde metamorphism, ductile deformation and brittle faulting that indicate continued deformation during exhumation of the Kampa Dome to shallower crustal levels. Structural, metamorphic and geochronologic datasets of the Kampa Dome are consistent with, but not necessarily unique to, the development of a southward-flowing mid-crustal channel beneath southern Tibet that was linked to surface denudation along the Himalayan range front, as predicted by ‘channel flow–extrusion’ models (Beaumont et al., 2001, 2004).

## Acknowledgments

We thank Jeff Lee for providing thorough and insightful comments that have greatly improved the presentation of our research from Kampa Dome. Jean-Pierre Burg and Bradley Hacker are also thanked for the instructive and detailed comments that improved both the clarity and quality of this manuscript. We thank Gordon Lister at Australia National University for providing financial and logistical assistance with U–Pb SHRIMP analyses and the Chinese Academy of Sciences for supporting our field work.

## Appendix A

Representative grains were carefully hand picked under a binocular microscope to avoid sample bias. Separates were mounted in epoxy resin and polished with alumina to expose grain interiors. Prior to analysis the zircon mounts were imaged using a cathodoluminescence (CL) detector at the Electron Microscopy Unit, ANU, with a HITACHI S2250-N SEM under 15 kV, ~60  $\mu\text{m}$ , and ~20 mm working distance operating conditions. CL imaging revealed internal zoning and structure within the zircons and served as a basis for selection of zircons for SHRIMP analyses.

U–Th–Pb analyses were conducted using SHRIMP Reverse geometry (RG) at the Research School of Earth Sciences, ANU. Instrumental conditions and data acquisition setup were generally as described by Compston et al. (1984) and Williams (1998), with isotope data collected from sets of six scans through the masses. The measured  $^{206}\text{Pb}/^{238}\text{U}$  ratios were corrected using the Temora zircon reference standard from the Middledale gabbroic diorite (Black et al., 2003). A zircon with a known U-content (SL13) was used as the U concentration standard for the unknowns. The data were treated following Compston et al. (1992). All analyses were corrected for common lead based on the measured  $^{208}\text{Pb}/^{206}\text{Pb}$  ratio calculated from the Th/U ratio, assuming equilibrium between the Th and U systems. This was satisfied by all analyses (with the exception of 2 metamict analyses) by plotting the Th/U versus  $^{208}\text{Pb}/^{206}\text{Pb}$  ratios. The  $^{208}\text{Pb}$  correction is well suited for highly radiogenic targets with a low Th/U such as the samples analysed here (GD25, Th/U < 0.8). The samples have moderate to high U-contents and a common lead content similar to that of the  $^{204}\text{Pb}$ -free standard. Therefore the measured common lead composition is assumed to be that

of the Broken Hill lead ( $^{207}\text{Pb}/^{206}\text{Pb} = 0.9618$ ,  $^{204}\text{Pb}/^{206}\text{Pb} = 0.0625$ ,  $^{208}\text{Pb}/^{206}\text{Pb} = 2.2285$ ), which approximates the laboratory surface common lead at ANU. Concordia age regression calculations from  $^{208}\text{Pb}$ -corrected isotope ratio data were carried out using Isoplot/Ex software (Ludwig, 2000).

## References

- Aitchison, J.C., Ali, J.R., Davis, A.M., 2007. When and where did India and Asia collide? *Journal of Geophysical Research* 112, B05423. doi:10.1029/2006JB004706.
- Aoya, M., Wallis, S.R., Terada, K., Lee, J., Kawakami, T., Wang, Y., Heizler, M., 2005. North–south extension in the Tibetan crust triggered by granite emplacement. *Geology* 33 (11), 853–856.
- Aoya, M., Wallis, S.R., Kawakami, T., Lee, J., Wang, Y., 2006. The Malashan metamorphic complex in southern Tibet: comparative study with Kangmar Dome with special reference to kinematics of deformation and origin of associated granites. In: Law, R.D., Searle, M.P., Godin, L. (Eds.), *Channel Flow, Ductile Extrusion and Exhumation of Lower-mid Crust in Continental Collision Zones*. Geological Society of London Special Publication, 268, pp. 471–496.
- Beaumont, C., Jamieson, R.A., Nguyen, M.H., Lee, B., 2001. Himalayan tectonics explained by extrusion of a low-viscosity crustal channel coupled to focused surface denudation. *Nature* 414, 738–742.
- Beaumont, C., Jamieson, R.A., Nguyen, M.H., Medvedev, S., 2004. Crustal channel flows: 1. Numerical models with applications to the tectonics of the Himalayan–Tibetan orogen. *Journal of Geophysical Research* 109, B06406. doi:10.1029/2003JB002809.
- Black, L.P., Kamo, S.L., Allen, C.M., Aleinkoff, J.N., Davis, D.W., Korsch, R.J., Foudoulis, C., 2003. TEMORA 1: a new zircon standard for Phanerozoic U–Pb geochronology. *Chemical Geology* 200, 155–170.
- Breeding, C., Ague, J., Grove, M., Rupke, A., 2004. Isotopic and chemical alteration of zircon by metamorphic fluids: U–Pb age depth-profiling of zircon crystals from Barrow’s garnet zone, northeast Scotland. *American Mineralogist* 89 (7), 1067–1077.
- Burchfiel, C., Royden, L., 1985. North–south extension within the convergent Himalayan region. *Geology* 13, 679–682.
- Burchfiel, B.C., Zhiliang, C., Hodges, K.V., Yuping, L., Royden, L.H., Changrong, D., Jiene, X., 1992. The south Tibetan detachment system, Himalayan orogen: extension contemporaneous with and parallel to shortening in a collisional mountain belt. *Geological Society America Special Paper* 269, 41.
- Burg, J.P., 1983. Carte géologique du sud du Tibet: Centre Nationale de la Recherche Scientifique, scale 1:500000.
- Burg, J.P., Guiraud, M., Chen, G.M., Li, G.C., 1984. Himalayan metamorphism and deformations in the north Himalayan Belt (southern Tibet, China). *Earth and Planetary Science Letters* 69, 391–400.
- Burg, J.P., Leyreloup, A., Girardeau, J., Chen, C.M., 1987. Structure and metamorphism of a tectonically thickened continental crust: the Yalu Tsango suture zone (Tibet). *Philosophical Transactions of the Royal Society of London* A321, 67–86.
- Chen, Z., Liu, Y., Hodges, K.V., Burchfiel, B.C., Royden, L.H., Deng, C., 1990. The Kangmar Dome: a metamorphic core complex in southern Xizang (Tibet). *Science* 250, 1552–1556.
- Compston, W., Williams, I.S., Meyer, C., 1984. U–Pb geochronology of zircons from lunar breccia 73217 using a sensitive high mass-resolution ion microprobe. *Journal of Geophysical Research* 89, B525–B534.
- Compston, W., Williams, I.S., Kirschvink, J.L., Zhang, Z., Ma, G., 1992. Zircon U–Pb ages for the Early Cambrian time-scale. *Journal of the Geological Society of London* 149, 171–184.
- Debon, F., Le Fort, P., Sheppard, S.M.F., Sonet, J., 1986. The four plutonic belts of the Transhimalaya–Himalaya: A chemical, mineralogical, isotopic, and chronological synthesis along a Tibet–Nepal section. *Journal of Petrology* 27, 219–250.
- Grujic, D., Casey, M., Davidson, C., Hollister, L., Kündig, R., Pavlis, T., Schmid, S., 1996. Ductile extrusion of the Higher Himalayan Crystalline in Bhutan: evidence from quartz microfabrics. *Tectonophysics* 260, 21–44.

- Hauck, M.L., Nelson, K.D., Brown, L.D., Zhao, W., Ross, A.R., 1998. Crustal structure of the Himalayan orogen at approximately 90° east longitude from Project INDEPTH deep reflection profiles. *Tectonics* 17, 481–500.
- Hirth, J.G., Tullis, J., 1991. The effect of porosity on the strength of quartz aggregates experimentally deformed in the dislocation creep regime. *Tectonophysics* 200, 97–110.
- Hirth, G., Tullis, J., 1992. Dislocation creep regimes in quartz aggregates. *Journal of Structural Geology* 14, 145–160.
- Hodges, K.V., 2000. Tectonics of the Himalayan and southern Tibet. *Geological Society of America Bulletin* 112, 324–350.
- Hodges, K.V., 2006. A synthesis of the Channel Flow — Extrusion hypothesis as developed for the Himalayan–Tibetan orogenic system. In: Law, R.D., Searle, M.P., Godin, L. (Eds.), *Channel Flow, Ductile Extrusion and Exhumation of Lower-mid Crust in Continental Collision Zones*. Geological Society of London Special Publication, 268, pp. 71–91.
- Hodges, K.V., Parrish, R.R., Searle, M.P., 1996. Tectonic evolution of the central Annapurna Range, Nepalese Himalayas. *Tectonics* 15, 1264–1291.
- Kawakami, T., Aoya, M., Wallis, S.R., Lee, J., Terada, K., Wang, Y., Heizler, M., 2007. Contact metamorphism in the Malashan Dome, North Himalayan gneiss domes, southern Tibet: an example of shallow extensional tectonics in the Tethys Himalaya. *Journal of Metamorphic Geology* 25, 831–853.
- Klootwijk, C., Gee, J., Pearce, J., Smith, G., McFadden, P., 1992. An early India–Asia contact; paleomagnetic constraints from Ninetyeast Ridge, ODP Leg 121; with Suppl. Data 92-15. *Geology* 20, 395–398.
- Lee, J., Whitehouse, M.J., 2007. Onset of mid-crustal extensional flow in southern Tibet: evidence from U/Pb zircon ages. *Geology* 35, 45–48.
- Lee, J., Dinklage, W.S., Hacker, B.R., Wang, Y., Gans, P.B., Calvert, A., Wan, J., Chen, W., Blythe, A., McClelland, W., 2000. Evolution of the Kangmar Dome, southern Tibet: structural, petrologic, and thermochronologic constraints. *Tectonics* 19, 872–896.
- Lee, J., Hacker, B., Wang, Y., 2004. Evolution of North Himalayan Gneiss Domes: structural and metamorphic studies in Mabja Dome, southern Tibet. *Journal of Structural Geology* 204, 2297–2316.
- Lee, J., McClelland, W., Wang, Y., Blythe, A., McWilliams, M., 2006. Oligocene–Miocene middle crustal flow in southern Tibet: geochronologic studies in Mabja Dome. In: Law, R.D., Searle, M.P., Godin, L. (Eds.), *Channel Flow, Ductile Extrusion and Exhumation of Lower-mid Crust in Continental Collision Zones*. Geological Society of London Special Publication, 268, pp. 445–470.
- Le Fort, P., 1986. Metamorphism and magmatism during the Himalayan collision. *Geological Society Special Publications* 19, 159–172.
- Le Fort, P., Cuney, M., Deniel, C., France-Lanord, C., Sheppard, S.M.F., Upreti, B.N., Vidal, P., 1987. Crustal generation of the Himalayan leucogranites. *Tectonophysics* 134, 39–57.
- Ludwig, K.R., 1998. On the treatment of concordant uranium-lead ages. *Geochimica et Cosmochimica Acta* 62, 665–676.
- Ludwig, K.R., 2000. Isoplot/Ex version 2.4, A geochronological toolkit for Microsoft Excel, Special Publication 56. Berkeley Geochron. Cent., Berkeley, Calif.
- Mattinson, J.M., Graubard, C.M., Parkinson, D.L., McClelland, W.C., 1996. U–Pb reverse discordance in zircons: the role of fine-scale oscillatory zoning and sub-micron transport of Pb. *Geophysical Monograph* 95, 355–370.
- Nelson, K.D., Zhao, W., Brown, L.D., Kuo, J., Che, J., Liu, X., Klempner, S.L., Makovsky, Y., Meissner, R., Mechier, J., Kind, R., Wenzel, F., Ni, J., Nabelek, J., Chen, L., Tan, H., Wei, W., Jones, A.G., Booker, J., Unsworth, M., Kidd, W.S.F., Hauck, M., Alsdorf, D., Ross, A., Cogan, M., Wu, C., Sandvol, E.A., Edwards, M., 1996. Partially molten middle crust beneath southern Tibet: synthesis of project INDEPTH results. *Science* 274, 1684–1688.
- Quigley, M.C., 2006. Continental tectonics and landscape evolution in south-central Australia and southern Tibet. Unpublished Ph.D. thesis, The University of Melbourne, 358 pp.
- Quigley, M., Yu Liangjun, Liu Xiaohan, Wilson, C.J.L., Sandford, M., Phillips, D., 2006.  $^{40}\text{Ar}/^{39}\text{Ar}$  thermochronology of the Kampa Dome, southern Tibet: implications for the thermal evolution of North Himalayan middle crust. *Tectonophysics* 421, 269–297.
- Ratschbache, L., Frisch, W., Liu, G., Chen, C., 1994. Distributed deformation in southern and western Tibet during and after the India–Asia collision. *Journal of Geophysical Research* 99, 19917–19945.
- Rubatto, D., Williams, I.S., Buick, I.S., 2001. Zircon and monazite response to prograde metamorphism in the Reynolds Range, central Australia. *Contributions to Mineralogy and Petrology* 140, 458–468.
- Schärer, U., Xu, R., Allegre, C., 1986. U–(Th)–Pb systematics and ages of Himalayan leucogranites, south Tibet. *Earth and Planetary Science Letters* 77, 35–48.
- Tullis, J., Yund, R.A., 1991. Experimental evidence for diffusion creep in feldspar aggregates. *Journal Structural Geology* 13, 987–1000.
- Vavra, G., Schmid, R., Gebauer, D., 1999. Internal morphology, habit and U–Th–Pb microanalysis of amphibolite-to-granulite facies zircons: geochronology of the Ivrea Zone (Southern Alps). *Contributions to Mineralogy and Petrology* 134, 380–404.
- Wallis, S.R., Aoya, M., Kawakami, T., Lee, J., Wang, Y., 2004. Dominant top-to-the-north deformation in the Malashan metamorphic dome and intrusive origin of associated granites in southern Tibet. In: Searle, M., Law, R., Godin, L. (Eds.), *Channel flow, Ductile Extrusion and Exhumation of Lower-mid Crust in Continental Collision Zones*, Geological Society of London Conference Programme and Abstracts.
- Watts, D.R., Harris, N., The 2002 NASA GLENN SOARS Working Group, 2005. Mapping granite and gneiss in domes along the North Himalayan antiform with ASTER SWIR band ratios. *GSA Bulletin* 117, 879–886.
- Williams, I.S., 1998. U–Th–Pb geochronology by ion microprobe. In: McKibben, M.A., Shanks III, W.C., Ridley, W.I. (Eds.), *Applications of Microanalytical Techniques to Understanding Mineralizing Processes*. *Reviews in Economic Geology*, 7, pp. 1–35.
- York, D., 1969. Least squares fitting of a straight line with correlated errors. *Earth and Planetary Science Letters* 5, 320–324.
- Zengqian, L., Shupe, J., Yifu, Z., Shaonian, Y., Changxing, A., Younian, Z., Yaomin, L., Huaida, W., Jian'e, X., Jingqing, H., Tieying, G., 1986. Geological map of Qinghai–Xizang (Tibet) Plateau and adjacent area. Chengdu Institute of Geological Sciences, Chinese Academy of Sciences, scale 1:150,000, 6 sheets.
- Zhang, Q., Zhou, Y., Li, D., Wu, H., 1986. Principal features of the gneissic dome and its peripheral metamorphic zones in Kangma of Xizang, China. *Scientia Geologica Sinica* 2, 125–133.
- Zhang, H., Harris, N., Parrish, R., Kelley, S., Li, Z., Rogers, N., Argles, T., King, J., 2004. Causes and consequences of protracted melting of the mid-crust exposed in the North Himalayan antiform. *Earth and Planetary Science Letters* 228, 195–212.
- Zhou, Y., Zhang, Q., Jin, C., Mei, H., 1981. Magmatism and Metamorphism in Xizang (Tibet): The Series of the Scientific Expedition to Qinghai–Xizang. Sci. Press, Beijing, p. 359.